



Available online at www.sciencedirect.com

ScienceDirect

Comput. Methods Appl. Mech. Engrg. 415 (2023) 116228

Computer methods in applied mechanics and engineering

www.elsevier.com/locate/cma

Stabilized formulation for phase-transforming flows with special emphasis on cavitation inception

Saikat Mukherjee*, Hector Gomez

Purdue University - School of Mechanical Engineering, 585 Purdue Mall, West Lafayette, 47907, IN, USA

Received 4 April 2023; received in revised form 27 June 2023; accepted 28 June 2023

Available online 13 July 2023

Abstract

Despite significant advancement in the field of cavitation, the inception of vapor bubbles from pure liquid is still not well understood. In this paper, we propose a numerical algorithm to solve the Navier–Stokes–Korteweg equations, which are phase-field equations that govern the dynamics of multiphase compressible flows. These equations can predict cavitation inception without phenomenological assumptions about mass transfer. We present a modification to the bulk free energy of the fluid that can help us simulate cavitation at much larger length scales than previously possible. We propose a numerical scheme based on a Taylor–Galerkin discretization, a residual-based discontinuity capturing operator and a spatial filtering scheme. Our numerical method can be used for high speed flows with large pressure gradients, which are distinctive features of flows where we observe cavitation inception. We present numerical examples that show the accuracy, stability and robustness of our scheme. Finally, we use the proposed numerical scheme to study benchmark problems in the field of cavitation inception such as flow past a wedge and flow past a bluff body. The proposed numerical scheme opens opportunities to understand different aspects of cavitation in general and inception in particular, in much more detail.

© 2023 Elsevier B.V. All rights reserved.

MSC: 0000: 1111

Keywords: Cavitation; Multiphase flows; Compressible flows; Navier-Stokes-Korteweg

1. Introduction

Many problems of fundamental interest and current research relevance involve phase-change of fluids from the liquid phase to the vapor phase, or vice-versa. Prime examples include designing heat-sinks for electronic devices [1], medical procedures such as cataract surgery and tissue emulsification [2] or tackling environmental issues such as waste management [3]. One of the prominent sub-categories of these phase-transforming flows is cavitating flows, where the conversion of a liquid to vapor is due to a reduction in pressure. The vapor bubbles generated by local depressurization can later expand and collapse based on local flow and pressure conditions. While the growth and shrinkage of these vapor bubbles has been extensively studied and is well understood, the formation of these vapor bubbles from the liquid, also known as cavitation inception, is not well understood. Most current numerical approaches use homogeneous mixture models, where the mixture of water and vapor are treated as either

E-mail address: mukher32@purdue.edu (S. Mukherjee).

^{*} Corresponding author.

incompressible phases [4–6], or as compressible phases with a constitutive equation of state [7,8]. Compressible models are considered more suitable for applications involving cavitation as they can capture the dynamics of condensation fronts in the fluid better than incompressible models [9,10]. These numerical approaches predict mass transfer between the phases by solving a separate transport equation for the mass fraction of vapor containing source terms. The source terms are phenomenological mass transfer functions, which predict the rate of conversion from liquid to vapor [11]. However, mass transfer functions cannot predict cavitation inception unambiguously.

An alternative approach that can be used to understand cavitating flows is through the Navier-Stokes-Korteweg (NSK) equations, which are based on the van der Waals (vdW) theory of phase transformations [12]. In this approach, the density of the fluid is a phase field, which indicates whether the fluid is in vapor or liquid phase. Because the method is based on the vdW theory of phase transformations, the bulk free energy of the fluid is a nonconvex function of the density in some regions of the phase diagram. The total free energy of the system is comprised of the bulk free energy and the interfacial free energy; and can be utilized to derive the governing equations using the Coleman-Noll procedure [13]. The interfacial energy is proportional to the square of the norm of the density gradient and manifests itself as third-order derivatives of the density in the linear momentum equation [14-16]. When the bulk free energy of the fluid is described by a non-convex function of density, the equilibrium density solution is comprised of a low density region, which describes the vapor state, and a higher density region which describes the liquid state of the fluid. No additional mass transfer functions are required to model the conversion of liquid to vapor, or vice versa. Thus, because the model encodes state of the art theory of phase transformations and does not require mass transfer functions with empirical parameters, it opens the possibility to more fundamental models of cavitation [17]. However, a major limitation of this approach is that, in its original form, it is only applicable to small-scale problems [18-21]. The reason for this is that the thickness of the liquid-vapor interface, which is in the order of nanometers at room temperature, needs to be resolved by the computational mesh [22,23]. Because of the structure of the equations, a naive enlargement of the interface would lead to a dramatic increase of surface tension that would render the model results meaningless [24]. However, it has been shown that the interface can be enlarged keeping surface tension constant [25-27]. Recent research [27] showed that a carefully designed interface enlargement approach combined with a stabilized algorithm can lead to a first-principles model of liquid-vapor flows. Because the approach relies on van der Waals theory only, we called it Direct van der Waals Simulation (DVS). Although DVS opens the possibility of high-fidelity prediction of liquid-vapor flows, it also comes with multiple challenges. One of them is that the isentropic form of the NSK equations is not hyperbolic in some regions of the phase diagram. This is problematic because most compressible flow solvers rely on the eigenstructure of the governing equations which is not available in this case, leading to partially ad-hoc numerical algorithms. Here, we address this challenge by deriving a stabilized formulation for DVS that does not rely on the eigenstructure of the equations. Our algorithm is based on a Taylor-Galerkin discretization [28-30] and a residual-based discontinuity capturing scheme inspired by Brenner's modification of the Navier-Stokes equations [31,32]. We also propose an interface enlargement technique based on a spline reconstruction of the equation of state (EoS) in the interfacial region. Our enlargement strategy produces surface tension errors smaller than 0.01% for a 108-fold enlargement, and leads to an EoS that is differentiable with respect to density. We found that the smoothness of the EoS significantly improves the stability of the algorithm.

Our discretization scheme and enlargement strategies are tested with multiple numerical tests, including manufactured solutions and cavitation problems at meter length scales. Overall, we feel that our methodology opens up new opportunities to better understand liquid–vapor flows at length scales relevant for engineering problems.

The rest of the paper is structured as follows. In Section 2, we provide an overview of the NSK equations and the free energy functional used to derive these equations. In Section 3, we describe our strategy to simulate physical phenomena at length scales several orders of magnitude larger than micron scale. In Section 4, we describe the details of our numerical scheme based on the Taylor–Galerkin method, a residual-based discontinuity capturing, and a filtering procedure based on [33]. The validation of our numerical scheme is provided in Section 5, where we provide tests of accuracy. Finally, we use our algorithm to study benchmark problems in cavitation inception such as flow past a wedge and flow past a square bluff body. We provide concluding remarks and future research aims in Section 6

2. Governing equations

The NSK equations constitute a phase-field model of liquid-vapor two-phase flows which accounts for the mass transfer in the fluid from liquid phase to vapor phase, or vice versa through a non-convex bulk free energy. They can

be understood as a regularization of the compressible Navier–Stokes equations for non-convex bulk free energies by considering additional stresses that take into account the variation of density in the interfacial region of the fluid. Here, we are interested in modeling cavitation inception, which is the initial formation and growth of vapor filled bubbles as a consequence of hydrodynamic forces. Thermal instabilities do not play a significant role during cavitation inception [34]. Hence, we consider the isothermal form of the NSK equations. The equations are as follows

$$\rho_t + \nabla \cdot (\rho \mathbf{u}) = 0,\tag{1}$$

$$(\rho \mathbf{u})_t + \nabla \cdot (\rho \mathbf{u} \otimes \mathbf{u} + p^{\text{EoS}} \mathbf{I}) - \nabla \cdot \mathbf{\tau} - \nabla \cdot \boldsymbol{\zeta_0} - \rho \mathbf{f} = 0, \tag{2}$$

where ρ is the density, u is the velocity, p^{EoS} is the pressure of the fluid and f represents a body force per unit mass. The subscript t represents the time derivative. The symbols τ and ζ_0 represent the viscous stress and the Korteweg stress tensors respectively and their expressions are as follows

$$\tau = \overline{\mu} (\nabla u + \nabla^T u) - \frac{2}{3} \overline{\mu} \nabla \cdot u I, \tag{3}$$

$$\boldsymbol{\zeta_0} = \lambda_0 \left(\rho \nabla^2 \rho + \frac{1}{2} |\nabla \rho|^2 \right) \boldsymbol{I} - \lambda_0 \nabla \rho \otimes \nabla \rho. \tag{4}$$

Here, $\overline{\mu}$ is the dynamic viscosity, and λ_0 is a positive constant that is proportional to the square of the thickness of the liquid-vapor interface. Eqs. (1)–(2) can be derived from the total free energy of the fluid — ensuring that it decreases with time and imposing constraints for the conservation of mass, linear and angular momentum using the Coleman-Noll procedure [35]. The total free energy of the fluid can be expressed as

$$\psi(\rho, \nabla \rho, \boldsymbol{u}) = \int_{\Omega} \left(\psi_{V}^{\text{EoS}}(\rho) + \frac{\lambda_{0}}{2} |\nabla \rho|^{2} + \frac{1}{2} \rho \boldsymbol{u}^{2} \right) d\Omega, \tag{5}$$

where $\frac{1}{2}\rho u^2$ is the kinetic energy per unit volume of the fluid. The term $\frac{\lambda_0}{2}|\nabla\rho|^2$ represents the free energy per unit volume at the interface between the liquid and vapor phases. The function $\psi_V^{\rm EoS}$ represents the bulk free energy per unit volume of the phase transforming liquid. Various models have been proposed in literature that describe this functional relationship [36,37]. In this paper, we use the van der Waals EoS to describe this functional relationship as follows

$$\psi_{V}^{EoS}(\rho) = R\theta\rho \log\left(\frac{\rho}{b-\rho}\right) - a(\theta)\rho^{2}.$$
 (6)

Here, θ is the temperature, R is the gas constant of the fluid, a and b are positive parameters from the vdW EoS that depend on the properties of the fluid and can be calculated using [38]

$$a(\theta) = \frac{27}{64} \frac{R^2 \theta_c^2}{p_c} \left\{ 1 + m \left(1 - \sqrt{\frac{\theta}{\theta_c}} \right) \right\}^2, \quad b = 8 \frac{p_c}{R\theta_c}. \tag{7}$$

Here, p_c and θ_c are respectively the critical pressure and critical temperature of the fluid. The constant m is the acentric factor of the fluid and is a measure of the non-sphericity of the fluid molecules, see [38] for values of m for different fluids. Since $\psi_V^{\rm EoS}$ is a non-convex function of ρ , for temperatures smaller than the critical temperature of the fluid, density solutions of Eqs. (1)–(2) separate into a low density region which represents the vapor phase and a high density region that represents the liquid phase. The pressure of the fluid is related to the bulk free energy per unit volume by the relation

$$p^{\text{EoS}} = \rho \frac{\partial \psi_{\text{V}}^{\text{EoS}}}{\partial \rho} - \psi_{\text{V}}^{\text{EoS}} = Rb\theta \frac{\rho}{b - \rho} - a(\theta)\rho^{2}. \tag{8}$$

The chemical potential can be expressed as

$$\mu^{\rm EoS} = \frac{\partial \psi_{\rm V}^{\rm EoS}}{\partial \rho} = R\theta b \log \left(\frac{\rho}{b - \rho} \right) + R\theta \frac{b}{b - \rho} - 2a(\theta)\rho. \tag{9}$$

The equilibrium solutions of Eqs. (1)–(2) for a particular θ in Cartesian coordinates correspond to density states which ensure mechanical equilibrium (same pressure) and chemical equilibrium (same chemical potential) between the liquid and vapor phases of the fluid. They can be derived from the Euler–Lagrange conditions of minimal free

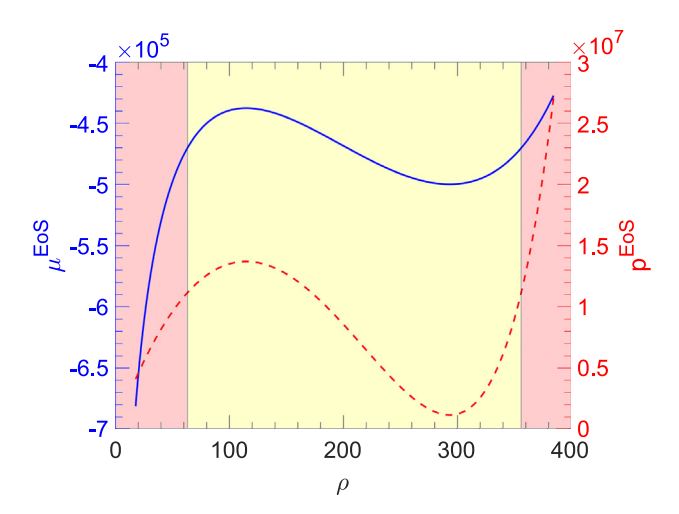


Fig. 1. Pressure and chemical potential for vdW EoS at $\theta = 550$ K. The two black vertical lines represent the equilibrium liquid and vapor densities and can be derived using Eq. (10). The yellow region represents the binodal zone. (For interpretation of the references to color in this figure legend, the reader is referred to the web version of this article.)

energy under the constraint of constant mass. Representing the equilibrium vapor density as ρ_v and the equilibrium liquid density as ρ_l , these conditions can be written as

$$Rb\theta \frac{\rho_v}{b - \rho_v} - a(\theta)\rho_v^2 = Rb\theta \frac{\rho_l}{b - \rho_l} - a(\theta)\rho_l^2, \tag{10}$$

$$R\theta b \log \left(\frac{\rho_v}{b - \rho_v}\right) + \frac{R\theta b}{b - \rho_v} - 2a(\theta)\rho_v = R\theta b \log \left(\frac{\rho_l}{b - \rho_l}\right) + \frac{R\theta b}{b - \rho_l} - 2a(\theta)\rho_l. \tag{11}$$

In Fig. 1, we plot μ^{EoS} (primary y-axis) and p^{EoS} (secondary y-axis) versus density at $\theta = 550$ K. The black vertical lines represent the equilibrium densities ($\rho_v = 63.1677 \text{ kg/m}^3$, $\rho_l = 355.8894 \text{ kg/m}^3$). The region of intermediate densities $\rho_v \leq \rho \leq \rho_l$ is represented in yellow and is also referred to as the binodal region .

3. Interface enlargement

Here, we present a new interface enlargement method for the NSK equations. An inherent property of the NSK equations as opposed to other phase-field models [39] is the relationship between the length scale of the interface thickness (which needs to be resolved by the mesh in a computation) and the surface tension. The constant λ_0 appearing in the free energy is proportional to the square of the interface thickness. However, as shown in [40], the liquid–vapor surface tension σ_{lv} is also related to λ_0 by

$$\sigma_{lv} = \int_{\rho_v}^{\rho_l} \sqrt{2\lambda_0 [\psi_V^{\text{EoS}}(\rho) - \psi_V^{\text{EoS}}(\rho_v) - \mu^{\text{sat}}(\rho - \rho_v)]} \, d\rho = \sqrt{2\lambda_0} F, \tag{12}$$

where $\mu^{\rm sat}$ is the equilibrium chemical potential and ρ_v is the equilibrium vapor density. The symbol F represents the contribution to the surface tension from the EoS, as it can be calculated directly from the EoS at a given temperature. Using Eq. (12), we can calculate the value of λ_0 for a fluid at a given temperature using the values of σ_{lv} . At room temperatures, the value of λ_0 obtained using Eq. (12), which is equal to 5.36×10^{-16} m⁷kg⁻¹s⁻² for water using the vdW EoS, corresponds to a liquid–vapor interface thickness of the order of nanometres. As phase-field models require an accurate resolution of the liquid–vapor interface, simulation of phase change phenomena at scales larger than the millimeter scale would require us to use more than $\sim 10^6$ elements per spatial dimension, which is numerically prohibitive even for simulations in two spatial dimensions. On the other hand, if we choose a large value of λ_0 , then the surface tension becomes nonphysically large and completely dominates other effects.

Existing work on enlarging the liquid-vapor interfacial zone while keeping intact the thermodynamic properties of the bulk phases has focused on increasing the capillary parameter λ_0 and modifying the EoS in the binodal region by decreasing F. In Fig. 2(a), we show the modification to the chemical potential in the binodal region

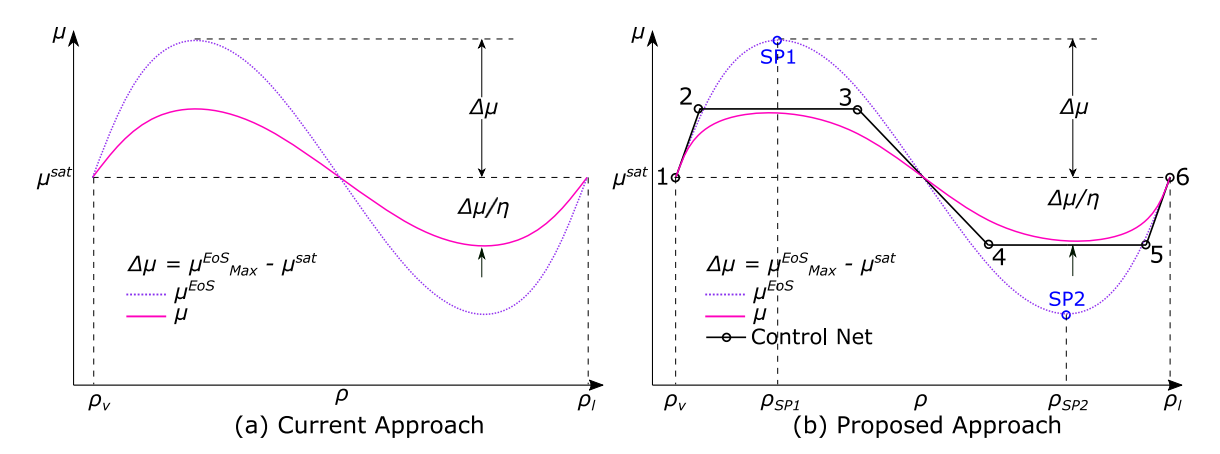


Fig. 2. (a) Modification of chemical potential in the binodal region [26] (b) Proposed modification in the binodal region using B-splines so that μ is differentiable.

as proposed in [26]. For a discussion on the implications of modifying the EoS in the interfacial region on the thermodynamic behavior of the fluid, see [25,26]. Here, η is the desired degree of interface enlargement, μ^{EoS} is the original chemical potential and μ is the modified chemical potential. Finally, $\Delta\mu$ is the difference between the maximum chemical potential in the binodal region ($\mu_{\text{Max}}^{\text{EoS}}$) and the equilibrium chemical potential (μ^{sat}). This approach has been successfully employed to study collision of droplets and evolution of jets at high Reynolds numbers in wall-free flows at temperatures close to the critical temperature for interface enlargement factors of up to 1000. However, a drawback of this approach is that the modified chemical potential is not differentiable with respect to density at the binodal boundaries. As the pressure is related to the chemical potential, this implies that the pressure is not a differentiable function of density across phase-boundaries. This becomes problematic when we are simulating advection dominated problems for large enlargement factors as additional smoothing in the interfacial region is required. To circumvent this issue, we propose a modification of the chemical potential in the binodal region using spline functions, as shown in Fig. 2(b). Our strategy is motivated by the approach in [41], where they derive an EoS for a phase transforming fluid by combining the ideal gas EoS for the vapor phase and the Tait EoS for the liquid phase. The use of splines allows them to combine two different EoS in a way that the resulting pressure is differentiable with respect to density. Here, we use splines to modify the EoS in the binodal region while keeping it unchanged outside of the binodal region and retaining the differentiability with respect to density. Before reconstructing, we calculate the equilibrium vapor and liquid densities (ρ_v and ρ_l respectively), the derivatives of the chemical potential using the EoS at binodal boundaries ($\frac{\partial \mu^{\rm EoS}}{\partial \rho}(\rho_v)$) and $\frac{\partial \mu^{\rm EoS}}{\partial \rho}(\rho_l)$) and $\Delta \mu$. Since ρ_l , ρ_v , $\frac{\partial \mu^{\rm EoS}}{\partial \rho}(\rho_v)$, $\frac{\partial \mu^{\mathrm{EoS}}}{\partial \rho}(\rho_l)$ and $\Delta \mu$ depend on the temperature of the fluid, our reconstruction assumes an isothermal liquid-vapor interface. However, this assumption is valid for the modeling of cavitation inception [34]. Points 1-6 in Fig. 2 represent the control points for the B-spline function [42]. The rationale to choose these points along with their coordinates can be found in Table 1. Here, ρ_{SP1} and ρ_{SP2} represent the densities at which μ^{EoS} attains extrema in the interval (ρ_v, ρ_l) . We use quadratic splines, and a uniform knot vector. Using this spline, we generate an approximation for the chemical potential in the binodal region which is differentiable across all densities, thereby alleviating the need for additional smoothing when solving the NSK equations for large interface enlargements. Using the modified chemical potential, we derive the free energy and pressure in the interfacial region through the relations

$$\psi_{\mathcal{V}}(\rho) = \psi_{\mathcal{V}}^{\text{EoS}}(\rho_{v}) + \int_{\rho_{v}}^{\rho} \mu d\rho, \tag{13}$$

$$p(\rho) = \begin{cases} \rho \mu - \psi_{V} & \text{if } \rho_{v} \le \rho \le \rho_{l} \\ p^{\text{EoS}} & \text{otherwise.} \end{cases}$$
 (14)

 (ρ_l, μ_{sat})

Control point #	Density	Chemical potential	Rationale
1	$ ho_v$	$\mu^{ m sat}$	Continuity of $\mu - \rho$ curve at (ρ_v, μ_{sat})
2	$ ho_v + rac{\Delta \mu}{\eta} / rac{\partial \mu^{ m EoS}}{\partial ho}(ho_v)$	$\mu^{\mathrm{sat}} + \frac{\Delta\mu}{\eta}$	Differentiability of $\mu - \rho$ curve at (ρ_n, μ_{sat})
3	$2\rho_{SP1}-\rho_2$	$\mu^{\mathrm{sat}} + \frac{\Delta\mu}{\eta}$	Density at extremum for $\mu - \rho$ curve remains same as
4	$2\rho_{SP2} - \rho_5$	$\mu^{\mathrm{sat}} - \frac{\Delta\mu}{\eta}$	$\mu^{\text{EoS}} - \rho$ curve Density at extremum for $\mu - \rho$ curve remains same as $\mu^{\text{EoS}} - \rho$ curve
5	$ ho_l - rac{\Delta \mu}{\eta} / rac{\partial \mu^{ m EoS}}{\partial ho}(ho_l)$	$\mu^{ m sat} - rac{\Delta \mu}{\eta}$	Differentiability of $\mu - \rho$ curve at (ρ_l, μ_{sat})
6	$ ho_l$	$\mu^{ m sat}$	Continuity of $\mu - \rho$ curve at

Table 1 Control points for the quadratic B-splines in Fig. 2(b). The knot vector is uniform

When derived in this way, the free energy is twice differentiable, and pressure and chemical potential are differentiable once with respect to density at the binodal densities. However, as we do not scale the chemical potential pointwise, the contribution to the surface tension from the modified EoS does not scale exactly as $\sqrt{\eta}$. In other words

$$\int_{\rho_{v}}^{\rho_{l}} \sqrt{\left[\psi_{V}^{EoS}(\rho) - \psi_{V}^{EoS}(\rho_{v}) - \mu^{sat}(\rho - \rho_{v})\right]} d\rho$$

$$\neq \sqrt{\eta} \int_{\rho_{v}}^{\rho_{l}} \sqrt{\left[\psi_{V}(\rho) - \psi_{V}^{EoS}(\rho_{v}) - \mu^{sat}(\rho - \rho_{v})\right]} d\rho.$$
(15)

Therefore, we evaluate the effective interface enlargement factor (η') utilizing the formula

$$\eta' = \left(\frac{\int_{\rho_v}^{\rho_l} \sqrt{[\psi_V^{EoS}(\rho) - \psi_V^{EoS}(\rho_v) - \mu^{sat}(\rho - \rho_v)]} d\rho}{\int_{\rho_v}^{\rho_l} \sqrt{[\psi_V(\rho) - \psi_V^{EoS}(\rho_v) - \mu^{sat}(\rho - \rho_v)]} d\rho}\right)^2.$$

$$(16)$$

Using Eq. (16), we modify the interfacial parameter in the binodal region as follows [26]

$$\lambda = \begin{cases} \eta' \lambda_0 & \text{if } \rho_v \le \rho \le \rho_l \\ \lambda_0 & \text{otherwise.} \end{cases}$$
 (17)

These two changes allow us to simulate phase change phenomena at large length scales. Therefore, our final governing equations after interface enlargement are

$$\rho_t + \nabla \cdot (\rho \mathbf{u}) = 0,\tag{18}$$

$$(\rho \mathbf{u})_t + \nabla \cdot (\rho \mathbf{u} \otimes \mathbf{u} + \rho \mathbf{I}) - \nabla \cdot \mathbf{\tau} - \nabla \cdot \boldsymbol{\zeta} - \rho \mathbf{f} = 0. \tag{19}$$

where ζ is the modified Korteweg stress tensor after interface enlargement

$$\boldsymbol{\zeta} = \lambda \left(\rho \nabla^2 \rho + \frac{1}{2} |\nabla \rho|^2 \right) \boldsymbol{I} - \lambda \nabla \rho \otimes \nabla \rho. \tag{20}$$

4. Numerical discretization

4.1. Split form of the governing equations

A major challenge in the numerical solution of NSK equations is the presence of third order derivatives of density in the momentum equation [43]. A commonly employed solution to this problem in finite elements involves splitting the higher order PDE into a system of lower order PDEs [44,45]. In this paper, we split the NSK equations into a system of lower order PDEs to simplify the implementation for spatial discretization using bilinear finite elements. Our governing equations are

$$\rho_t + \nabla \cdot (\rho \mathbf{u}) = 0, \tag{21}$$

$$(\rho \mathbf{u})_t + \nabla \cdot (\rho \mathbf{u} \otimes \mathbf{u} + \rho \mathbf{I}) - \nabla \cdot \mathbf{\tau} - \nabla \cdot \boldsymbol{\zeta} - \rho \mathbf{f} = 0, \tag{22}$$

$$\nu - \nabla^2 \rho = 0,\tag{23}$$

where the viscous tensor τ and pressure p follow from Eqs. (3) and (14) respectively. The Korteweg stress term ζ becomes

$$\boldsymbol{\zeta} = \lambda \left(\rho \nu + \frac{1}{2} |\nabla \rho|^2\right) \boldsymbol{I} - \lambda \nabla \rho \otimes \nabla \rho. \tag{24}$$

4.2. Time discretization of the Navier-Stokes-Korteweg equations

In this paper, we develop a numerical procedure to solve the NSK equations for scenarios involving cavitation, which are often characterized by high speeds. Solutions to advection dominated transport problems by the Galerkin method are frequently contaminated by oscillations [46]. Although they can be removed by drastic spatial and temporal refinement, their practical utility is severely undermined. Most stabilized numerical formulations to solve the compressible Navier-Stokes equations use the speed of sound in the fluid to design stabilization terms for advection dominated flows and shocks. The speed of sound is equal to the square root of the slope of the pressure density curve under isentropic conditions, which is positive for commonly used pressure-density relations such as ideal gas law or stiffened fluid law. However, the non-convex relationship between the bulk free energy and density, which is essential to model phase transformations, implies that the pressure decreases with an increase in density in the spinodal region for cubic equations of state such as the vdW EoS under isentropic conditions. Hence, standard stabilized algorithms for compressible flows such as SUPG [47], VMS [48] or Galerkin Least squares [49] cannot be applied directly for the solution of NSK equations. One way to deal with this problem is to use the Taylor-Galerkin discretization scheme for developing a stabilized numerical formulation. This approach has been widely used to solve a plethora of advection dominated transport problems [30,50-52]. In this method, we use forward-time Taylor series expansions to discretize in time first, leaving the spatial variable continuous. The spatial variable is discretized afterwards using the regular Galerkin approach, and combined together this is referred to as the Taylor-Galerkin method [28,29,53]. Since we use the governing equations and Taylor series expansions, this method provides numerical stability without relying on the eigenstructure of the equations. In this section, we explain our time discretization scheme for the NSK equations. Using Taylor series expansion, we can write

$$\rho^n = \rho - \Delta t \rho_t + \frac{\Delta t^2}{2} \rho_{tt} + \Theta(\Delta t^3), \tag{25}$$

$$(\rho \mathbf{u})^n = (\rho \mathbf{u}) - \Delta t (\rho \mathbf{u})_t + \frac{\Delta t^2}{2} (\rho \mathbf{u})_{tt} + \Theta(\Delta t^3), \tag{26}$$

where the superscript n represents the value at the previous timestep, whereas the variables without superscripts represent values at $t^{n+1} = t^n + \Delta t$. Rearranging terms, we can write

$$\rho_t = \frac{1}{\Delta t} \left(\rho - \rho^n \right) + \frac{\Delta t}{2} \rho_{tt} + \Theta(\Delta t^2), \tag{27}$$

$$(\rho \mathbf{u})_t = \frac{1}{\Delta t} \left[(\rho \mathbf{u}) - (\rho \mathbf{u})^n \right] + \frac{\Delta t}{2} (\rho \mathbf{u})_{tt} + \Theta(\Delta t^2). \tag{28}$$

Taking the time derivative of mass conservation and momentum balance from Eqs. (21)-(22), we get

$$\rho_{tt} = -\nabla \cdot (\rho_t \mathbf{u} + \rho \mathbf{u}_t),
(\rho \mathbf{u})_{tt} = -\nabla \cdot (\rho_t \mathbf{u} \otimes \mathbf{u} + \rho \mathbf{u}_t \otimes \mathbf{u} + \rho \mathbf{u} \otimes \mathbf{u}_t + p_\rho \rho_t \mathbf{I}) + \overline{\mu} \nabla \cdot (\nabla \mathbf{u}_t + \nabla^T \mathbf{u}_t)
- \frac{2}{3} \overline{\mu} \nabla \cdot \mathbf{u}_t \mathbf{I} + \lambda \nabla \cdot \left[(\rho_t \nu + \rho \nu_t + \nabla \rho \cdot \nabla \rho_t) \mathbf{I} - \nabla \rho_t \otimes \nabla \rho - \nabla \rho \otimes \nabla \rho_t \right]
+ \rho_t \mathbf{f} + \rho \mathbf{f}_t,$$
(30)

where $p_{\rho} = \partial p/\partial \rho$. Substituting ρ_{tt} and $(\rho u)_{tt}$ from Eqs. (29) and (30) in Eqs. (27)–(28) respectively; ρ_{t} and $(\rho u)_{t}$ from Eqs. (21)–(23) in Eqs. (27)–(28), and using backward Euler approximation for the other time derivatives, we

obtain our time-discretized governing equations

$$\frac{1}{\Delta t} \left(\rho - \rho^{n} \right) - \frac{1}{2} \nabla \cdot \left[(\rho - \rho^{n}) \boldsymbol{u} + \rho (\boldsymbol{u} - \boldsymbol{u}^{n}) \right] + \nabla \cdot (\rho \boldsymbol{u}) = 0, \tag{31}$$

$$\frac{1}{\Delta t} \left[(\rho \boldsymbol{u}) - (\rho \boldsymbol{u})^{n} \right] - \frac{1}{2} \nabla \cdot \left[(\rho - \rho^{n}) \boldsymbol{u} \otimes \boldsymbol{u} + \rho (\boldsymbol{u} - \boldsymbol{u}^{n}) \otimes \boldsymbol{u} + \rho \boldsymbol{u} \otimes (\boldsymbol{u} - \boldsymbol{u}^{n}) \right]$$

$$- \frac{1}{2} \nabla \cdot \left[p_{\rho} (\rho - \rho^{n}) \boldsymbol{I} \right] + \frac{\overline{\mu}}{2} \nabla \cdot \left[\nabla \left(\boldsymbol{u} - \boldsymbol{u}^{n} \right) + \nabla^{T} \left(\boldsymbol{u} - \boldsymbol{u}^{n} \right) - \frac{2}{3} \nabla \cdot \left(\boldsymbol{u} - \boldsymbol{u}^{n} \right) \boldsymbol{I} \right]$$

$$+ \frac{\lambda}{2} \nabla \cdot \left[-\nabla \left(\rho - \rho^{n} \right) \otimes \nabla \rho - \nabla \rho \otimes \nabla \left(\rho - \rho^{n} \right) + \left\{ \left(\rho - \rho^{n} \right) \boldsymbol{v} + \rho \left(\boldsymbol{v} - \boldsymbol{v}^{n} \right) \right\} \boldsymbol{I} \right]$$

$$+ \frac{\lambda}{2} \nabla \cdot \left[\nabla \rho \cdot \nabla \left(\rho - \rho^{n} \right) \boldsymbol{I} \right] + \frac{1}{2} \left[(\rho - \rho^{n}) \boldsymbol{f} + \rho (\boldsymbol{f} - \boldsymbol{f}^{n}) \right] + \nabla \cdot (\rho \boldsymbol{u} \otimes \boldsymbol{u} + p \boldsymbol{I})$$

$$- \nabla \cdot \boldsymbol{\tau} - \nabla \cdot \boldsymbol{\xi} - \rho \boldsymbol{f} = 0,$$

$$(32)$$

$$v - \nabla^{2} \rho = 0.$$

4.3. Weak form of the time discretized problem

We use bilinear finite elements for spatial discretization. We start by deriving a weak form of the problem. Let $X \in H^1(\Omega)$ denote both the trial and weighting function space, which are assumed to be identical. Here, $H^1(\Omega)$ represents the standard Sobolev space of square-integrable functions with square-integrable first order derivatives. Let $(\cdot, \cdot)_{\Omega}$ denote the \mathcal{L}^2 inner product with respect to the domain Ω . The variational problem is: Find $U = \{\rho, \mathbf{u}, \mathbf{v}\} \in X$ such that $\forall W = \{q, \mathbf{w}, \phi\} \in X$,

$$B(\mathbf{W}, \mathbf{U}) = 0, (34)$$

where

$$B(W, U) = B_{NSK}^{TG}(W, U) + B_{NSK}^{Sponge}(W, U) + B_{NSK}^{DC}(W, U).$$
(35)

Here, $B_{\rm NSK}^{\rm TG}$ is the contribution to the weak form that ensures the weak satisfaction of Eqs. (31)–(33). $B_{\rm NSK}^{\rm Sponge}$ is used to enforce outflow and inflow boundary conditions for some of the simulations in this paper, whereas $B_{\rm NSK}^{\rm DC}$ is used to add discontinuity capturing to prevent oscillations when steep density and velocity gradients are present in the solution. Under the assumption of periodic boundary conditions in all directions, we get

$$B_{\text{NSK}}^{\text{TG}}(\boldsymbol{W}, \boldsymbol{U}) = \left(q, \frac{1}{\Delta t}(\rho - \rho^{n})\right)_{\Omega} - (\nabla q, \rho \boldsymbol{u})_{\Omega} + \frac{1}{2} (\nabla q, \boldsymbol{u}(\rho - \rho^{n}))_{\Omega}$$

$$+ \frac{1}{2} (\nabla q, \rho (\boldsymbol{u} - \boldsymbol{u}^{n}))_{\Omega} + (\boldsymbol{w}, \frac{1}{\Delta t}(\rho \boldsymbol{u} - \rho^{n} \boldsymbol{u}^{n}))_{\Omega}$$

$$- (\nabla \boldsymbol{w}, \rho \boldsymbol{u} \otimes \boldsymbol{u})_{\Omega} - (\nabla \cdot \boldsymbol{w}, p)_{\Omega} + (\nabla \boldsymbol{w}, \boldsymbol{\tau})_{\Omega} - \lambda (\nabla \boldsymbol{w}, \nabla \rho \otimes \nabla \rho)_{\Omega}$$

$$+ \lambda (\nabla \cdot \boldsymbol{w}, \rho \boldsymbol{v})_{\Omega} + \frac{\lambda}{2} (\nabla \cdot \boldsymbol{w}, |\nabla \rho|^{2})_{\Omega} - (\boldsymbol{w}, \rho \boldsymbol{f})_{\Omega}$$

$$+ \frac{1}{2} (\nabla \boldsymbol{w}, (\rho - \rho^{n}) \boldsymbol{u} \otimes \boldsymbol{u})_{\Omega} + \frac{1}{2} (\nabla \boldsymbol{w}, \rho (\boldsymbol{u} - \boldsymbol{u}^{n}) \otimes \boldsymbol{u})_{\Omega}$$

$$+ \frac{1}{2} (\nabla \boldsymbol{w}, \rho \boldsymbol{u} \otimes (\boldsymbol{u} - \boldsymbol{u}^{n}))_{\Omega} + \frac{1}{2} (\nabla \cdot \boldsymbol{w}, p_{\rho}(\rho - \rho^{n}))_{\Omega}$$

$$- \frac{\overline{\mu}}{2} (\nabla \boldsymbol{w}, \nabla (\boldsymbol{u} - \boldsymbol{u}^{n}) + \nabla^{T} (\boldsymbol{u} - \boldsymbol{u}^{n}))_{\Omega} + \frac{\overline{\mu}}{3} (\nabla \cdot \boldsymbol{w}, \nabla \cdot (\boldsymbol{u} - \boldsymbol{u}^{n}))_{\Omega}$$

$$+ \frac{\lambda}{2} (\nabla \boldsymbol{w}, (\nabla \rho - \nabla \rho^{n}) \otimes \nabla \rho)_{\Omega} + \frac{\lambda}{2} (\nabla \boldsymbol{w}, \nabla \rho \otimes (\nabla \rho - \nabla \rho^{n}))_{\Omega}$$

$$- \frac{\lambda}{2} (\nabla \cdot \boldsymbol{w}, (\rho - \rho^{n}) \boldsymbol{v})_{\Omega} - \frac{\lambda}{2} (\nabla \cdot \boldsymbol{w}, \rho (\boldsymbol{v} - \boldsymbol{v}^{n}))_{\Omega}$$

$$- \frac{\lambda}{2} (\nabla \cdot \boldsymbol{w}, (\rho - \rho^{n}) \boldsymbol{v})_{\Omega} - \frac{\lambda}{2} (\nabla \cdot \boldsymbol{w}, \rho (\boldsymbol{v} - \boldsymbol{v}^{n}))_{\Omega}$$

$$+ \frac{1}{2} (\boldsymbol{w}, \rho (\boldsymbol{f} - \boldsymbol{f}^{n}))_{\Omega} + (\phi, \boldsymbol{v})_{\Omega} + (\nabla \phi, \nabla \boldsymbol{v})_{\Omega}.$$
(36)

In addition to periodic, Dirichlet and 90° contact angle boundary conditions ($\nabla \rho \cdot \mathbf{n} = 0$, where \mathbf{n} represents the unit vector along the normal to the surface) that are naturally imposed by $B_{\rm NSK}^{\rm TG}$, we also impose sponge boundary conditions for some simulations in this paper. This boundary condition is commonly employed for compressible flow simulations to prevent reflections from outflow boundaries [54]. This additional component to the variational formulation can be expressed as

$$B_{\text{NSK}}^{\text{Sponge}}(\boldsymbol{W}, \boldsymbol{U}) = (q, \delta(\rho - \rho_0))_{\mathcal{O}} + (\boldsymbol{w}, \delta(\rho \boldsymbol{u} - \rho_0 \boldsymbol{u}_0))_{\mathcal{O}}, \tag{37}$$

where $\delta(x)$ is a Heaviside function of space that is 0 outside the sponge region and 1 inside it. In our simulations, we approximate the Heaviside function with a hyperbolic tangent. The use of a smooth approximation for δ improves the numerical results. In Eq. (37), ρ_0 and u_0 are the far field density and velocity respectively.

Solutions to compressible flow problems with phase change have steep density and velocity gradients. Therefore, a discontinuity capturing (DC) scheme is implemented to prevent spurious oscillations in the solution. We use a residual-based discontinuity capturing scheme based on Brenner's modifications to the Navier–Stokes equations [31]. We use an isothermal version of the scheme proposed in [32]. First, we calculate the residuals of the time-discrete balance laws for mass and momentum given by Eqs. (31)–(32),

$$R_{\rho} = \frac{1}{\Delta t} (\rho - \rho^{n}) - \frac{1}{2} \nabla \cdot \left[(\rho - \rho^{n}) \mathbf{u} + \rho (\mathbf{u} - \mathbf{u}^{n}) \right] + \nabla \cdot (\rho \mathbf{u}),$$

$$R_{\mathbf{u}} = \frac{1}{\Delta t} \left[(\rho \mathbf{u}) - (\rho \mathbf{u})^{n} \right] - \frac{1}{2} \nabla \cdot \left[(\rho - \rho^{n}) \mathbf{u} \otimes \mathbf{u} + \rho (\mathbf{u} - \mathbf{u}^{n}) \otimes \mathbf{u} \right]$$

$$- \frac{1}{2} \nabla \cdot \left[\rho \mathbf{u} \otimes (\mathbf{u} - \mathbf{u}^{n}) + p_{\rho} (\rho - \rho^{n}) \mathbf{I} \right] + \frac{\overline{\mu}}{2} \nabla \cdot \left[\nabla \left(\mathbf{u} - \mathbf{u}^{n} \right) + \nabla^{T} \left(\mathbf{u} - \mathbf{u}^{n} \right) \right]$$

$$- \frac{\overline{\mu}}{3} \nabla \cdot \left[\nabla \cdot \left(\mathbf{u} - \mathbf{u}^{n} \right) \mathbf{I} \right] + \frac{\lambda}{2} \nabla \cdot \left[-\nabla \left(\rho - \rho^{n} \right) \otimes \nabla \rho - \nabla \rho \otimes \nabla \left(\rho - \rho^{n} \right) \right]$$

$$+ \frac{\lambda}{2} \nabla \cdot \left[\left[\left(\rho - \rho^{n} \right) \nu + \rho \left(\nu - \nu^{n} \right) + \nabla \rho \cdot \nabla \left(\rho - \rho^{n} \right) \right] \mathbf{I} \right]$$

$$+ \frac{1}{2} \left[(\rho - \rho^{n}) \mathbf{f} + \rho (\mathbf{f} - \mathbf{f}^{n}) \right] + \nabla \cdot (\rho \mathbf{u} \otimes \mathbf{u} + \rho \mathbf{I}) - \nabla \cdot \boldsymbol{\tau} - \nabla \cdot \boldsymbol{\zeta} - \rho \mathbf{f}.$$
(39)

We use R_{ρ} and R_{u} to calculate our discontinuity capturing residual vector

$$\mathbf{R}_{\mathbf{DC}} = \{ R_{\rho} \ R_{u} \}. \tag{40}$$

We use the norm of R_{DC} to obtain the DC viscosity coefficient using

$$\mu_{\rm DC} = \frac{1}{2} \Delta x^2 \| \mathbf{R}_{\rm DC} \|_2,\tag{41}$$

where Δx is a representative element size. For more details on the element size chosen for discontinuity capturing for non-uniform meshes, see Section 5. Then, we evaluate the contribution of DC to our weak form using

$$B_{\text{NSK}}^{\text{DC}} = \left(\nabla q, \frac{C_{\rho}\mu_{\text{DC}}}{\rho}\nabla\rho\right)_{\Omega} + \left(\nabla \boldsymbol{w}, \frac{4}{3}\mu_{\text{DC}}\nabla\boldsymbol{u}\right)_{\Omega} + \left(\nabla \boldsymbol{w}, \frac{C_{\rho}\mu_{\text{DC}}}{\rho}\boldsymbol{u}\otimes\nabla\rho\right)_{\Omega},\tag{42}$$

where C_{ρ} is a positive constant. Unless otherwise stated, we use $C_{\rho} = 0.01$ throughout this paper.

4.4. Spatial discretization

For spatial discretization, we use the Galerkin method. We derive the following problem over the finite element space X^h : find $U^h = \{\rho^h, u^h, v^h\} \in X^h \subset X$ such that $\forall W^h = \{q^h, w^h, \phi^h\} \in X^h \subset X$,

$$B(\mathbf{W}^h, \mathbf{U}^h) = 0, (43)$$

where \mathbf{W}^h and \mathbf{U}^h are defined as

$$U^{h} = \{\rho^{h}, u^{h}, v^{h}\}, \qquad \rho^{h} = \sum_{A=1}^{n_{b}} \rho_{A}(t) N_{A}(x),$$

$$u^{h} = \sum_{A=1}^{n_{b}} u_{A}(t) N_{A}(x), \qquad v^{h} = \sum_{A=1}^{n_{b}} v_{A}(t) N_{A}(x),$$
(44)

$$\mathbf{W}^{h} = \{q^{h}, \mathbf{w}^{h}, \phi^{h}\}, \qquad q^{h} = \sum_{A=1}^{n_{b}} q_{A}(t) N_{A}(\mathbf{x}),$$

$$\mathbf{w}^{h} = \sum_{A=1}^{n_{b}} \mathbf{w}_{A}(t) N_{A}(\mathbf{x}), \quad \phi^{h} = \sum_{A=1}^{n_{b}} \phi_{A}(t) N_{A}(\mathbf{x}).$$
(45)

In Eqs. (44)–(45), the N_A 's are basis functions that span X^h and n_b is the dimension of our discrete space. Throughout this paper, we use bilinear basis functions on quadrilateral meshes.

4.5. Numerical implementation

Let A be the global node index. The vector \mathbf{e}_i denotes the ith Cartesian basis vector. Let \mathbf{V} denote the vector of global degrees of freedom. We define the following residual vectors: $\mathbf{R}^C = \{R_A^C\}, \mathbf{R}^M = \{R_A^M\}, \mathbf{R}^P = \{R_A^P\}, \text{ such that } \mathbf{r}^P = \{R_A^P\}, \mathbf{r}^P = \{R_A^$

$$R_A^C = B(\{N_A, 0, 0\}, \{\rho^h, \mathbf{u}^h, \nu^h\}), \tag{46}$$

$$R_{Ai}^{M} = B(\{0, N_{A}\boldsymbol{e}_{i}, 0\}, \{\rho^{h}, \boldsymbol{u}^{h}, \nu^{h}\}), \tag{47}$$

$$R_A^P = B(\{0, 0, N_A\}, \{\rho^h, \mathbf{u}^h, \nu^h\}), \tag{48}$$

and $\mathbf{R} = \{\mathbf{R}^C, \mathbf{R}^M, \mathbf{R}^P\}$. The algorithm can be formulated as follows: Given V_n and $\Delta t = t_{n+1} - t_n$, find V_{n+1} such that

$$R(V_{n+1}) = 0,$$
 (49)

where the nonlinear system in Eq. (49) is linearized using Newton's method. Although the Taylor-Galerkin discretization provides stability in advection-dominated problems, we found that it is not sufficiently robust for challenging problems. Hence, after every nonlinear iteration, we use a filtering procedure to guarantee accuracy and stability by applying artificial viscosity locally [33,55,56]. Let Ω_i represent an element ($i \in 1, ..., N_{el}$), where N_{el} represents the total number of elements in our computational mesh. Let N_i represent the set of neighboring elements that share an edge with Ω_i . The set N_i is defined as $N_i = \{N_i^j\}$, $j = 1, ..., n_n$, where n_n represents the number of neighboring elements. Let n_q represent the total number of quadrature points per element, and x_i^q represent the coordinates of the qth quadrature point in the ith element of the mesh. Then, our algorithm for spatial filtering comprises the following steps:

1. Compute element averaged quantities for the element Ω_i using the expressions

$$\boldsymbol{x}_{\Omega_{i}} = \frac{1}{n_{q}} \sum_{q=1}^{n_{q}} \boldsymbol{x}_{i}^{q}, \qquad \rho_{\Omega_{i}} = \frac{1}{n_{q}} \sum_{q=1}^{n_{q}} \rho(\boldsymbol{x}_{i}^{q}), \quad \nabla \rho_{\Omega_{i}} = \frac{1}{n_{q}} \sum_{q=1}^{n_{q}} \nabla \rho(\boldsymbol{x}_{i}^{q}),$$

$$\boldsymbol{u}_{\Omega_{i}} = \frac{1}{n_{q}} \sum_{q=1}^{n_{q}} \boldsymbol{u}(\boldsymbol{x}_{i}^{q}), \quad \nu_{\Omega_{i}} = \frac{1}{n_{q}} \sum_{q=1}^{n_{q}} \nu(\boldsymbol{x}_{i}^{q}).$$

$$(50)$$

2. Compute $\tilde{\rho}(x_i^q)$ at each quadrature point through the equations

$$\tilde{\rho}(\mathbf{x}_i^q) = \rho(\mathbf{x}_i^q) + \frac{1}{n_n} \sum_{i=1}^{n_n} \left[\nabla \rho_{\Omega_j} \left(\mathbf{x}_{\Omega_j} - \mathbf{x}_i^q \right) - \left(\rho_{\Omega_j} - \rho(\mathbf{x}_i^q) \right) \right]. \tag{51}$$

3. Estimate the unit normal to the two-phase interface at every quadrature point using

$$\mathbf{n}(\mathbf{x}_i^q) = \frac{\nabla \rho(\mathbf{x}_i^q)}{|\nabla \rho(\mathbf{x}_i^q)|}$$
 with $\mathbf{n}(\mathbf{x}_i^q) = \mathbf{0}$ if $\nabla \rho(\mathbf{x}_i^q) = \mathbf{0}$.

4. Compute the density sensor $S^{\rho}(\mathbf{x}_{i}^{q})$ at each quadrature point using

$$S^{\rho}(\boldsymbol{x}_{i}^{q}) = \frac{|\boldsymbol{u}(\boldsymbol{x}_{i}^{q}) \cdot \boldsymbol{n}(\boldsymbol{x}_{i}^{q})|\Delta t}{\Delta x} \left| \frac{\tilde{\rho}(\boldsymbol{x}_{i}^{q}) - \rho(\boldsymbol{x}_{i}^{q})}{0.01\rho(\boldsymbol{x}_{i}^{q})} \right|. \tag{52}$$

5. Compute element averaged density sensor as

$$S_{\Omega_i}^{\rho} = \frac{1}{n_q} \sum_{q=1}^{n_q} S^{\rho}(\mathbf{x}_i^q). \tag{53}$$

6. Compute the filtered values at quadrature points using

$$\rho^F(\mathbf{x}_i^q) = \rho(\mathbf{x}_i^q) - \frac{1}{n_n} \sum_{i=1}^{n_n} \left(\rho_{\Omega_j} - \rho(\mathbf{x}_i^q) \right) S_{\Omega_j}^{\rho}$$
(54)

$$\boldsymbol{u}^{F}(\boldsymbol{x}_{i}^{q}) = \frac{1}{\rho^{F}(\boldsymbol{x}_{i}^{q})} \left[\rho(\boldsymbol{x}_{i}^{q}) \boldsymbol{u}(\boldsymbol{x}_{i}^{q}) - \frac{1}{n_{n}} \sum_{j=1}^{n_{n}} \boldsymbol{u}_{\Omega_{j}} \left(\rho_{\Omega_{j}} - \rho(\boldsymbol{x}_{i}^{q}) \right) S_{\Omega_{j}}^{\rho} \right]$$
(55)

$$\nu^{F}(\mathbf{x}_{i}^{q}) = \nu(\mathbf{x}_{i}^{q}) - \frac{1}{n_{n}} \sum_{i=1}^{n_{n}} \left(\nu_{\Omega_{j}} - \nu(\mathbf{x}_{i}^{q}) \right) S_{\Omega_{j}}^{\rho}.$$
 (56)

7. Substitute the values at quadrature points with the filtered values

We use the filtered values to compute the residual in Eq. (49) for the next nonlinear iteration.

5. Results

5.1. Accuracy tests

In this section, we use manufactured solutions to estimate the rate of convergence of our spatial discretization. First, we define a 1D manufactured solution on the computational domain $\Omega = (0, 1)$ m. We select an exact smooth solution that satisfies periodic boundary conditions

$$\rho(x,t) = 494.0658 + 29.56\sin(5\pi t)\cos(2\pi x) \text{ kg m}^{-3},$$
(57)

$$u(x,t) = \sin(3\pi t)\sin(2\pi x) \text{ ms}^{-1},$$
 (58)

and Eqs. (21)–(23) for a particular force f. The force term f is obtained by inserting the solution given by Eqs. (57)–(58) in Eqs. (21)–(23). For this particular force f, our numerical scheme should produce approximations to the exact solution from Eqs. (57)–(58). In this section, we study the rate of change of the numerical error as we refine in space. We consider water, and take $\theta = 300$ K, $\overline{\mu} = 10^{-3}$ Pa s, $\lambda_0 = 5.36 \times 10^{-16}$ m⁷kg⁻¹s⁻², a = 1848.8894 m⁵ kg⁻¹ s⁻², b = 591.2 kg/m³, $C_{\rho} = 0.01$ and $\eta = 50$. We use our proposed algorithm to solve Eqs. (21)–(23) on several grids, with uniform discretization in space using linear elements for all refinement levels. We choose $\Delta t = 10^{-7}$ s for the simulations in this 1D accuracy test, as there is no significant change in the results when we reduce the timestep from $\Delta t = 10^{-7}$ s to $\Delta t = 10^{-8}$ s for all refinement levels. In Fig. 3(a), we plot the \mathcal{L}^2 norm of the numerical error at t = 0.1 s corresponding to different refinement levels. Our results suggest optimal rate of convergence.

Then, we estimate the rate of convergence using a 2D manufactured solution. Our manufactured solution, which satisfies periodic boundary conditions on the computational domain $\Omega = (0, 1) \times (0, 1)$ m, is

$$\rho(x, y, t) = 494.0658 + 29.56 \sin(5\pi t) \cos(2\pi x) \cos(2\pi y) \text{ kg m}^{-3},$$
(59)

$$u(x, y, t) = \sin(3\pi t)\sin(2\pi x)\sin(2\pi y) \quad \text{ms}^{-1},$$
(60)

$$v(x, y, t) = \sin(\pi t)\sin(4\pi x)\sin(4\pi y) \text{ ms}^{-1}.$$
 (61)

We obtain the force term f by following the same procedure as the 1D case, and we use the same physical parameters θ , $\overline{\mu}$, λ , a, b, C_{ρ} and η . Again, we solve Eqs. (21)–(23) on several grids, with uniform discretization in space using bilinear elements for all refinement levels. We choose $\Delta t = 10^{-6}$ s, as the change in our solution is very small on reducing the timestep from $\Delta t = 10^{-6}$ s to $\Delta t = 10^{-7}$ s. In Fig. 3(b), we plot the \mathcal{L}^2 norm of the error at t = 0.1 s. Again, our results indicate optimal rate of convergence.

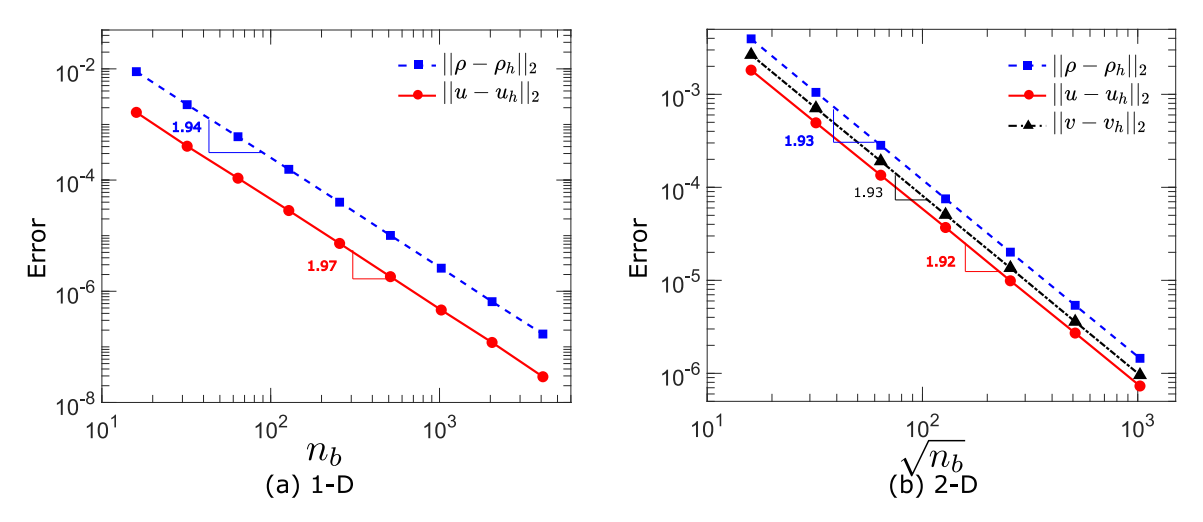


Fig. 3. \mathcal{L}^2 norm of the error for different number of elements. The order of accuracy is indicated next to the error norm line. The scheme is almost second order accurate.

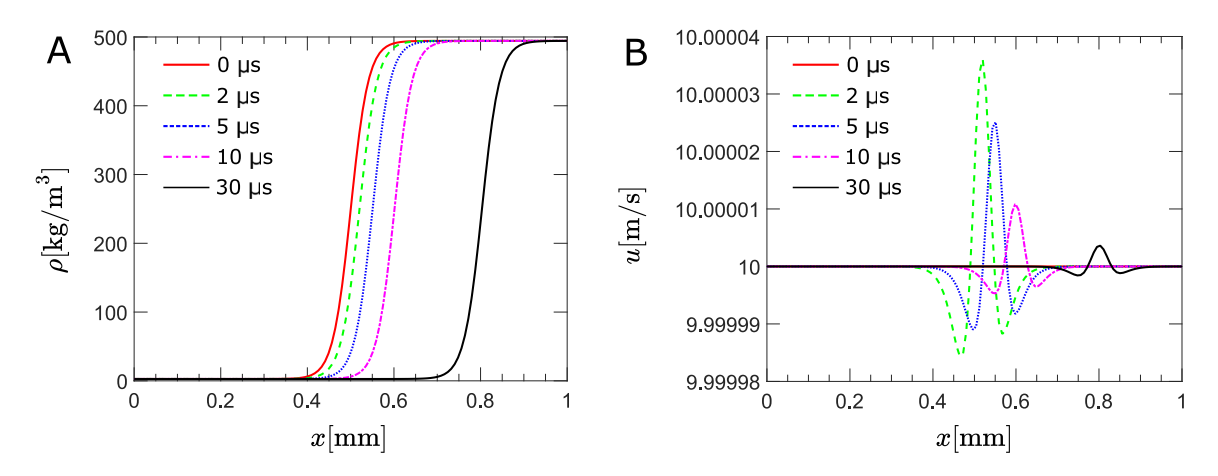


Fig. 4. Density (A) and velocity (B) plots for the propagation of a liquid-vapor interface in water at room temperature at t = 0, 2, 5, 10 and 30 μ s.

5.2. Propagation of a liquid-vapor interface at constant velocity

In this section, we study the propagation of a liquid-vapor interface in water at room temperature in a one-dimensional simulation, when subjected to Dirichlet boundary conditions on both sides. We take $\theta=300$ K, $\overline{\mu}=10^{-3}$ Pa s, $\lambda_0=5.36\times10^{-16}$ m⁷kg⁻¹s⁻², a=1848.8894 m⁵ kg⁻¹ s⁻², b=591.2 kg/m³, $C_{\rho}=0.01$ and $\eta=10^4$. Our computational domain is $x\in(0,1)$ mm, with Dirichlet boundary conditions $\rho=2.6916$ kg/m³ and u=10 m/s at x=0; and $\rho=494.0630$ kg/m³ and u=10 m/s at x=1 mm. The Reynolds number based on the length of the domain and the liquid density is 4940.63. Our initial conditions are

$$\rho(x,0) = 248.3773 + 245.6857 \tanh \{64000(x - 0.0005)\} \text{ kg m}^{-3}, \tag{62}$$

$$\mathbf{u}(x,0) = 10 \text{ ms}^{-1}.$$
 (63)

We use a uniform mesh in space with 128 linear elements, and take $\Delta t = 10^{-8}$ s. In Fig. 4, we plot the evolution of the density (A) and velocity (B) as the wave propagates across the domain. Since the initial density profile is not in equilibrium, we observe oscillations of the order of 10^{-3} % in the velocity field at t = 2 μ s. These oscillations reduce in magnitude as the wave propagates through the fluid to $\sim 5 \times 10^{-5}$ % at t = 30 μ s. This shows the stabilizing effect of our algorithm for advection dominated flows.

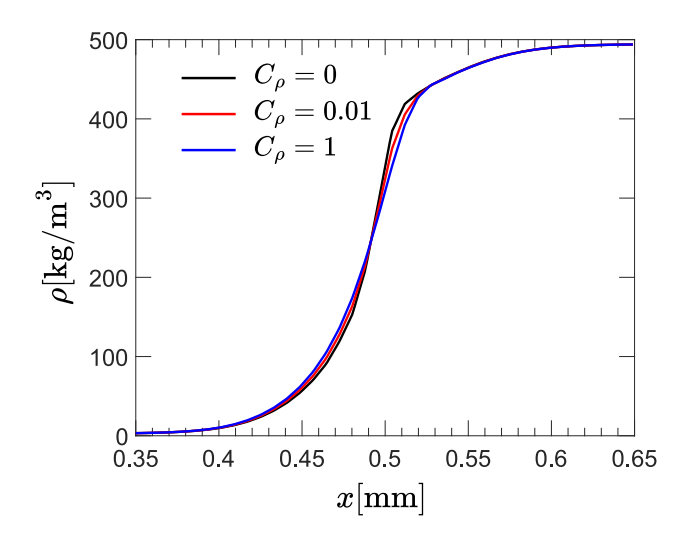


Fig. 5. Equilibrium density profile in one-dimensional Cartesian coordinates using $C_{\rho} = 0$, 0.01 and 1.

5.3. Effect of discontinuity capturing on equilibrium solutions

In this section, we study the impact of varying the discontinuity capturing parameter on two-phase equilibrium solutions of water at room temperature. We take $\theta=300$ K, $\overline{\mu}=10^{-3}$ Pa s, $\lambda_0=5.36\times10^{-16}$ m⁷kg⁻¹s⁻², a=1848.8894 m⁵ kg⁻¹ s⁻², b=591.2 kg/m³ and $\eta=10^4$. We run three simulations with $C_{\rho}=0$, 0.01 and 1. Our computational domain is $x\in(0,1)$ mm, with Dirichlet boundary conditions $\rho=2.6916$ kg/m³ and u=0 at x=0; and $\rho=494.0630$ kg/m³ and u=0 at x=1 mm. Our initial conditions are

$$\rho(x,0) = 248.3773 + 245.6857 \tanh \{64000(x - 0.0005)\} \text{ kg m}^{-3}, \tag{64}$$

$$\mathbf{u}(x,0) = 0 \text{ ms}^{-1}.$$
 (65)

We use a uniform mesh in space for all three cases with 512 linear elements, and take $\Delta t = 10^{-8}$ s. This is the same spatial resolution across the interface that we use for simulating cavitation in Sections 5.5–5.6. We run the simulations till $t = 10^{-2}$ s, when the $\|u\|_2 < 10^{-10}$ m/s, which we use as criterion for an equilibrium solution. In Fig. 5, we plot the density profiles in the interval $x \in (0.35, 0.65)$ mm at $t = 10^{-2}$ s. The density profiles far away from the interface are indistinguishable for all cases, but the jump from vapor to liquid density is steeper for $C_{\rho} = 0$ as compared to $C_{\rho} = 1$. We conclude that the values of C_{ρ} do not produce a significant change in the equilibrium solutions.

5.4. Oscillation of a liquid-vapor interface in an inviscid fluid

A flat two-phase interface initially deformed by a harmonic longitudinal perturbation oscillates indefinitely in an inviscid isothermal fluid when not subjected to any external forces. When the amplitude of the applied perturbation is small, the linear theory of small amplitude oscillations can be used to derive the following relationship between the frequency of oscillation of the interface (ω) and the wavenumber of the initial perturbation (k) [57]

$$\omega^2 = \frac{(\rho_B - \rho_t)gk + \sigma_{lv}k^3}{\rho_B \coth(kh_B) + \rho_t \coth(kh_T)},\tag{66}$$

where ρ_B , ρ_t and h_B , h_T are respectively the densities and heights of the liquid below and above the interface. The symbol g represents the acceleration due to gravity. In the absence of viscosity and heat transfer, numerical diffusion is the only dissipative mechanism that can reduce the amplitude of an initial perturbation to the liquid-vapor interface. Here, we simulate the oscillation of an interface that contains liquid nitrogen on one side, and nitrogen in vapor form on the other side. We consider the case with no gravity, therefore g = 0. The parameters for our simulation are $\overline{\mu} = 0$ Pa s, $\lambda_0 = 10^{-16}$ m⁷kg⁻¹s⁻², $C_\rho = 0.01$ and $\eta = 50$. We use the Soave-Redlich-Koang

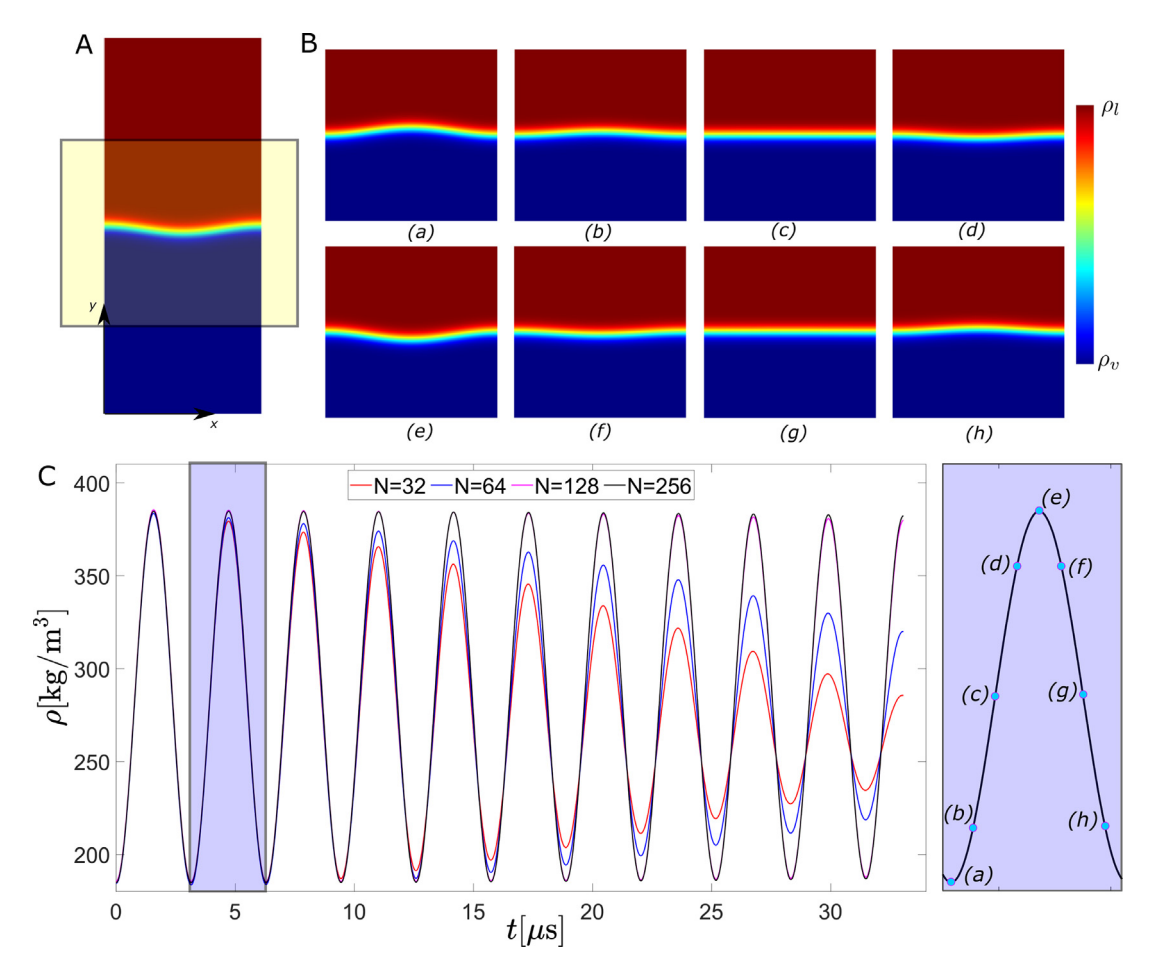


Fig. 6. (A) Computational domain for the simulation of an inviscid multiphase oscillating fluid interface. (B) Snapshots of density at $t = t_0$ (a), $9/8t_0$ (b), $10/8t_0$ (c), $11/8t_0$ (d), $12/8t_0$ (e), $13/8t_0$ (f), $14/8t_0$ (g), and $15/8t_0$ (h). (C) Evolution of density at the center of the domain $(l_0/2, 3/2l_0)$ for N = 32, 64, 128 and 256. The density oscillations decay with time for small N, whereas they do not decay for large values of N.

(SRK) EoS [58] to simulate nitrogen at $\theta = 119.88$ K, for which $\rho_l = 458.94$ kg m⁻³ and $\rho_v = 125.22$ kg m⁻³. We choose the same parameters for the SRK EoS as the interface oscillation example in [26]. Our computational domain is a rectangle as shown in Fig. 6A, with a width of $l_0 = 4849.12$ nm and height $3l_0$. The initial height of the fluids below and above the interface are equal $(h_B = h_T = 1.5l_0)$, and the densities at the top and bottom are equal to the saturation vapor and liquid densities. The flat interface is initially deformed by one period of a sinusoidal deformation $(k = 2\pi/l_0)$, with a small amplitude $0.05l_b$. Corresponding to this setup and domain dimensions, the time period of oscillation can be expressed using Eq. (66) as

$$t_o = \frac{l_0^{3/2}}{\sigma_{lv}^{1/2}} \sqrt{\frac{\coth(1.5)(\rho_l + \rho_v)}{2\pi}}.$$
 (67)

The time period t_0 depends on the width of the domain, the liquid-vapor surface tension and the saturation liquid and vapor densities. Substituting the values for nitrogen at 119.88 K, we get $t_0 = 3.1512 \,\mu s$. Our initial condition can be represented mathematically as

$$\rho(x, y) = \frac{1}{2}(\rho_l + \rho_v) - \frac{1}{2}(\rho_l - \rho_v) \tanh\left\{\frac{y - 1.5l_0 - w_0 [1 - \cos(2\pi x)]}{w_0}\right\},$$

$$\mathbf{u} = \mathbf{0},$$
(68)

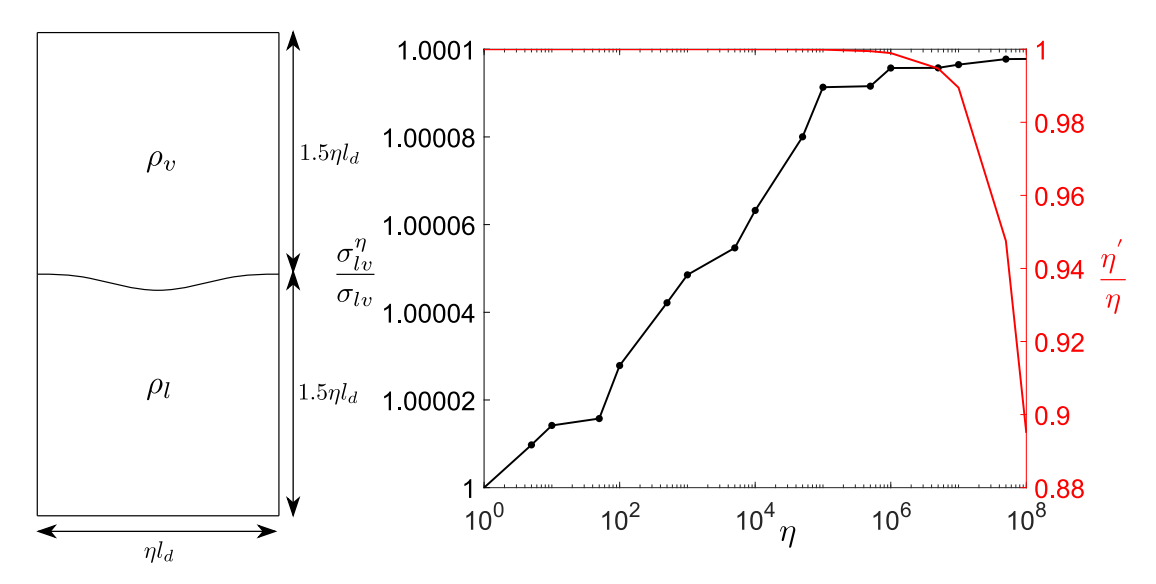


Fig. 7. (Left) Computational domain to determine the effect of interface enlargement parameter η on the liquid–vapor surface tension. (Right) Plot of $\sigma_{lv}^{\eta}/\sigma_{lv}$ (black) and η'/η (red) versus η . (For interpretation of the references to color in this figure legend, the reader is referred to the web version of this article.)

where $w_0 = 317$ nm is the approximate thickness of the liquid-vapor interface. We employ free-slip and 90° contact angle boundary conditions along the entire boundary. We use uniform meshing in space, with N bilinear elements along the x-direction and 3N elements along the y-direction, so that $n_b = 3N^2$. For all simulations in this section, we take $\Delta t = 10^{-8}$ s. In Fig. 6B, we show the contours of density in the region shown in yellow in Fig. 6A for N = 256. The interface between the liquid and the vapor phases changes gradually from concave upwards to concave downwards as we advance in time during the first half of a single cycle of oscillation from $t = t_0$ to $t = 1.5t_0$, and then again transforms from concave downwards to concave upwards from $t = 1.5t_0$ to $t = 2t_0$. The oscillation of the interface continues indefinitely in time with no discernible change in the amplitude of oscillations.

Next, we use this example to study the dissipation introduced by our numerical scheme as we coarsen our computational grid in space. We solve the problem on three different computational grids, with N=32, 64 and 128 and compare the data with the results for N=256. For comparison, we plot the density at the center of our domain $(l_0/2, 3l_0/2)$ versus time for different values of N in Fig. 6C. The amplitude of oscillation of density at the center decays with time, implying numerical dissipation is large for N=32 and N=64. However, the amplitude of the oscillation remains almost unchanged for N=128. The time period for oscillation is the same for all cases and does not depend on the spatial discretization. The observed time period is 3.14 μ s, which is within a $\sim 0.3\%$ deviation from the theoretically predicted value. The results are almost identical for N=128 and N=256, which shows that the numerical dissipation becomes negligible as we refine in space.

Next, we use this theoretical solution to determine the effective surface tension that we observe in our simulations for different values of η . Since we do not use pointwise scaling for the chemical potential while modifying the EoS as discussed in Section 3, the effective factor of interface enlargement η' obtained is not exactly equal to η , but is slightly smaller. However, the surface tension should remain unchanged irrespectively of the value of η , which we test using simulations here. While modifying the EoS, we do not change the liquid and vapor saturation densities ρ_l and ρ_v . Therefore, the time period of oscillation of the interface in Eq. (67) depends only on the width of the domain and the actual surface tension. Our simulation setup is described in Fig. 7. Here, $l_d = 96.9824$ nm is the width of the domain for $\eta = 1$. We vary the domain width by varying η . Representing σ_{lv}^{η} as the effective surface tension and t_{η} as the time period of oscillation for an interface enlargement factor η , we can write using Eq. (67)

$$\frac{t_1}{t_\eta} = \left(\frac{l_d}{\eta l_d}\right)^{3/2} \left(\frac{\sigma_{lv}^{\eta}}{\sigma_{lv}}\right)^{1/2}.\tag{69}$$

In Fig. 7, we plot the observed value of $\sigma_{lv}^{\eta}/\sigma_{lv}$ from our simulations versus the interface enlargement factor η . We also plot the value of η'/η versus η , which we calculate using Eq. (16) to show the efficiency of our interface

Fig. 8. Computational domain and boundary conditions for flow past a wedge. The lengths are in meters. The yellow region indicates the part of the domain shown in Figs. 9–10. (For interpretation of the references to color in this figure legend, the reader is referred to the web version of this article.)

Table 2 Size of the first element in metres along the positive (δx^+) and negative (δx^-) x-direction from the apex of the wedge and the growth factor for different number of total number of elements.

N_x	δx^+	δx^-	Growth factor (κ)
64	0.008922972	0.019247324	1.05
128	0.000938908	0.005377826	1.05
256	1.26577×10^{-5}	0.000673498	1.05
512	2.36027×10^{-9}	1.333×10^{-5}	1.05

enlargement procedure for large values of η . We observe that the percentage error in the surface tension estimation is less than 0.01% for η values up to 10^8 , which is quite negligible and shows the strength of the proposed method. The ratio η'/η decreases as we increase the value of η , showing that the procedure is less effective for larger values of η . However, the ratio is about 0.9 for $\eta=10^8$, implying a reduction of only 10% when we are simulating interface thicknesses of the order of centimetres.

5.5. Cavitating flow over a wedge

Flow over a wedge is a benchmark problem in the field of cavitation that has been well studied numerically [59, 60], experimentally [61,62] and analytically [63,64]. When a flowing fluid detaches from a solid surface, there is a reduction in pressure downstream which leads to the onset of cavitation. Here, we use our numerical model to study cavitating flow of water past a wedge in 2D at constant temperatures. We use the van der Waals fluid model for water and assume a constant temperature $\theta = 300$ K for the simulations in this section, for which a = 1848.8894 m⁵ kg⁻¹ s⁻² and b = 591.2 kg/m³. Our computational domain and boundary conditions are shown in Fig. 8. The computational domain is extended in both upstream and downstream directions from the wedge to minimize the impact of acoustic reflection from the boundaries [59]. In the sponge region at the inlet, we specify our free stream velocity $u_0 = (7.9, 0)$ m/s and free stream density ($\rho_0 = 1.016667\rho_l$), whereas we only specify the free stream density in the sponge region near the outlet. We use the acoustically absorbing boundary conditions in the sponge region. At the top and bottom boundaries, we impose a contact angle of 90°. The bottom wall is a no-slip wall, whereas we specify a velocity equal to the free stream velocity at the top wall. Our initial condition can be represented mathematically as

$$\rho(x, y, 0) = \rho_0 \text{ kg m}^{-3}, \quad \mathbf{u}(x, y, 0) = \left(7.9 \left(\frac{y}{0.125}\right)^2, 0\right) \text{ ms}^{-1}.$$
 (70)

For all the results shown here, we take $\overline{\mu}=10^{-3}$ Pa s, $\lambda_0=5.36\times10^{-16}$ m⁷kg⁻¹s⁻², $C_\rho=0.01$ and $\eta=10^6$. First, we study whether the solutions obtained using our algorithm converge when we refine spatially. We employ three different meshes composed of 64^2 , 128^2 and 256^2 bilinear elements. The mesh size is uniform along the vertical direction, implying $\Delta y=0.125/N_y$, where N_y is the number of elements along the y-direction. Along the x-direction, the elements are smaller near the apex of the wedge and become larger as we move farther away from the apex. In Table 2, we summarize our parameters for constructing the grid along the x-direction for different values of N_x . The symbol δx^+ represents the size of the first element along the positive x-direction, whereas δx^- represents the size of the first element along the negative x-direction measured from the apex of the wedge. The growth factor is the same along both directions. Our element size for discontinuity capturing is the element size

in the vertical direction $\Delta y = 0.125/N_y$. We keep our timestep constant equal to $\Delta t = 10^{-5}$ s for all the above simulations. In Fig. 9, we plot the density contours for the simulations at t = 0.05, t = 0.15 and t = 0.25 s respectively. The results are nearly identical, but the transition of density from vapor to liquid regions becomes smoother as we refine in space. This is due to the presence of more elements along the two phase interface. For a more quantitative point by point comparison, we compare the densities along the trailing edge of the wedge. In Fig. 9, we also plot the densities along the trailing edge of the wedge at t = 0.05, 0.15 and 0.25 s. At t = 0.05, the results are almost identical for all element sizes, but the difference is more pronounced as we march forward in time. There is a slight variation when we go from N = 64 to 128, but the results are almost identical for N = 128 and 256, proving that our algorithm converges to a solution when we refine spatially.

Next, we use the algorithm to study the features of cavitating flow past a wedge. For this study, we use N=512, with the mesh parameters as mentioned in Table 2. All other physical parameters remain identical. In Fig. 10, we plot the time evolution of the density field. At t=0, the domain is filled with liquid with uniform density ρ_0 . The flow accelerates in the convergent portion of the wedge which causes a reduction in pressure. The maximum reduction in pressure is observed at the apex of the wedge (not shown). At t=0.005 s, we observe a vapor cavity near the apex of the wedge. This is a major strength of the proposed model over existing mass transfer models [59,65], as it can predict conversion to vapor even when no vapor is initially present. With passage of time, this initially small vapor cavity keeps growing further along the direction of the flow without getting detached from the trailing edge of the wedge. As the free stream velocity is very high, turbulence and advection effects are dominant in addition to phase change and surface tension. At t=0.025 s, we observe a splitting of the original bubble into 2 bubbles, which grow and coalesce at t=0.05 s, and again split at t=0.075 s. The region of maximum phase change is focused near the apex of the wedge till t=0.1 s, and we do not observe detachment of bubbles from the bottom wall. The observations are very similar to experimental observations of sheet cavitation in flow past a wedge experiments, albeit they are three dimensional experiments and these simulations are performed in two dimensions.

In the second column of Fig. 10, we plot the evolution of the density field after t = 0.125 s where the growth of the vapor cavity is not limited only to the direction of the flow. The cavity gradually detaches from the trailing edge of the wedge at t = 0.15 s. At t = 0.175 s, some cavities detach completely from the trailing edge of the wedge and appear as vapor bubbles in the liquid. These clouds of vapor are then convected along the flow from t = 0.2 to t = 0.25 s. The density inside these clouds is much lower than the density in the sheets of vapor in Fig. 10, which is consistent with experiments and previous numerical simulations [59,61]. In these latter stages, our observations are qualitatively similar to cloud cavitation as observed in three dimensional experiments of cavitation in flow past a wedge.

5.6. Flow past a solid square

Flow past a solid square is an example [66,67] where cavitation inception occurs due to flow separation by the bluff body. These flows have been investigated extensively, especially for cylindrical and square obstacles owing to the vortices formed in the wake of the solid body. Therefore, there is a lot of experimental and numerical data [68–70], especially for non-cavitating scenarios. However, the liquid in the neighborhood of the solid obstacle can get converted into vapor if the pressure falls below a certain threshold value [71]. The presence of these vaporous regions in addition to turbulence makes the numerical study of these flows very challenging. Here, we use our model to study this phenomena of cavitating flow of water behind a solid square obstacle at room temperature. Our fluid model and temperature are the same as in Section 5.5. Our computational domain and boundary conditions are shown in Fig. 11. The solid square, shown in black in Fig. 11 is placed slightly below the line of symmetry to aid the formation of vortices from the start of the simulation. We impose the free stream velocity $u_0 = (7.9, 0)$ m/s and density ($\rho_0 = 1.0166667\rho_l$) at the inlet boundary and the density at the outlet (ρ_0) using sponge boundary conditions. At the top and bottom boundaries and on the surface of the solid, we impose no slip and 90° contact angle boundary conditions. Our initial conditions can be represented mathematically as

$$\rho(x, y, 0) = \rho_0 \text{ kg m}^{-3}, \quad \mathbf{u}(x, y, 0) = \left(7.9 \frac{y}{0.04} \left(1 - \frac{y}{0.04}\right), 0\right) \text{ ms}^{-1}.$$
 (71)

For all the results shown here, we take $\overline{\mu}=10^{-3}$ Pa s, $\lambda_0=5.36\times10^{-16}$ m⁷kg⁻¹s⁻², $C_\rho=0.01$ and $\eta=10^6$. The mesh is comprised of 512^2 bilinear elements, with more refinement around the solid square. The characteristic mesh size for discontinuity capturing is taken as 7.8125×10^{-5} m. We take a constant timestep of $\Delta t=10^{-5}$ s. In Fig. 12,

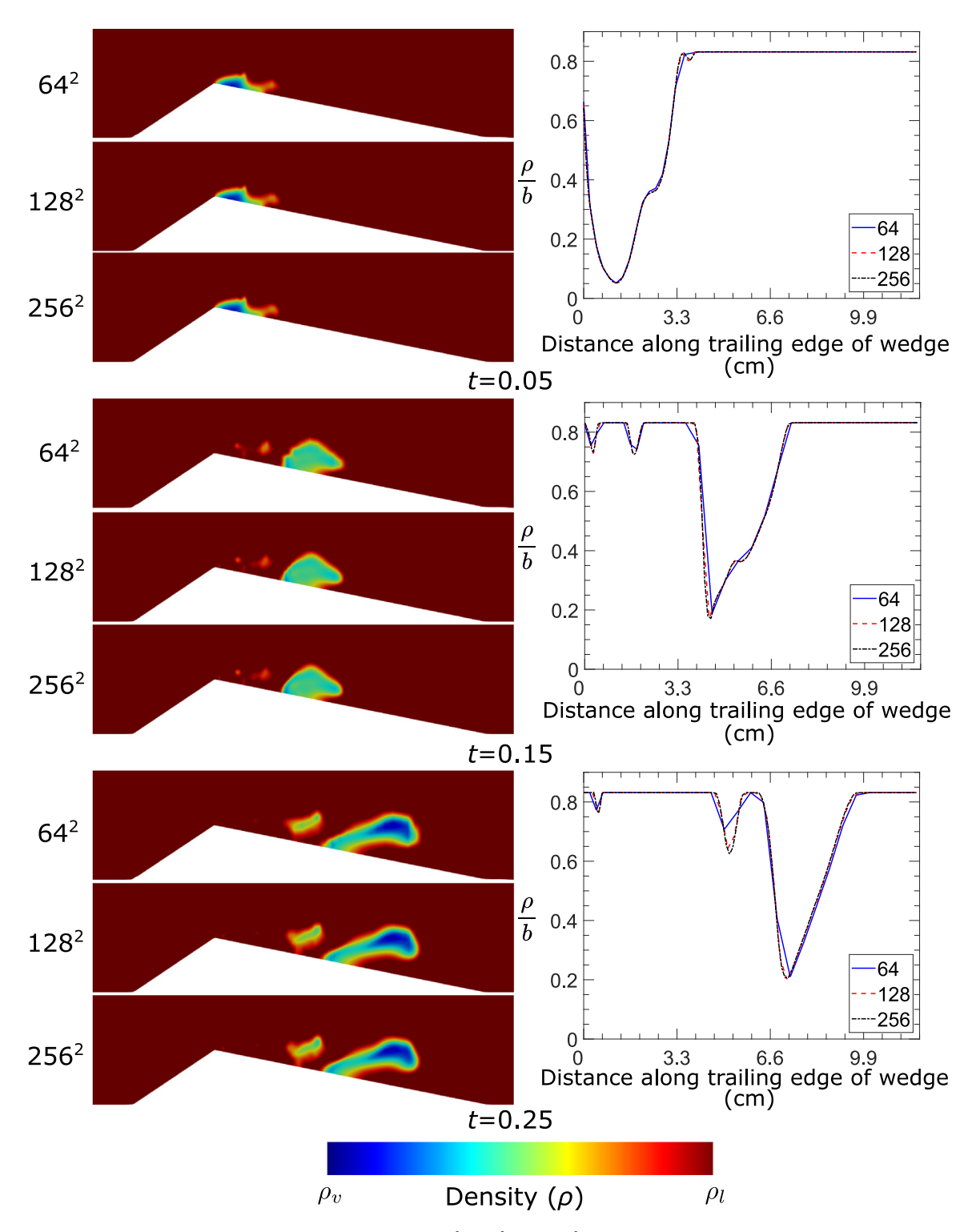


Fig. 9. (Left) Density contours for flow past a wedge using 64^2 , 128^2 and 256^2 elements at t = 0.05, 0.15 and 0.25 s. (Right) Density variation along the trailing edge of the wedge, measured from the apex of the wedge for the three different meshes. (For interpretation of the references to color in this figure legend, the reader is referred to the web version of this article.)

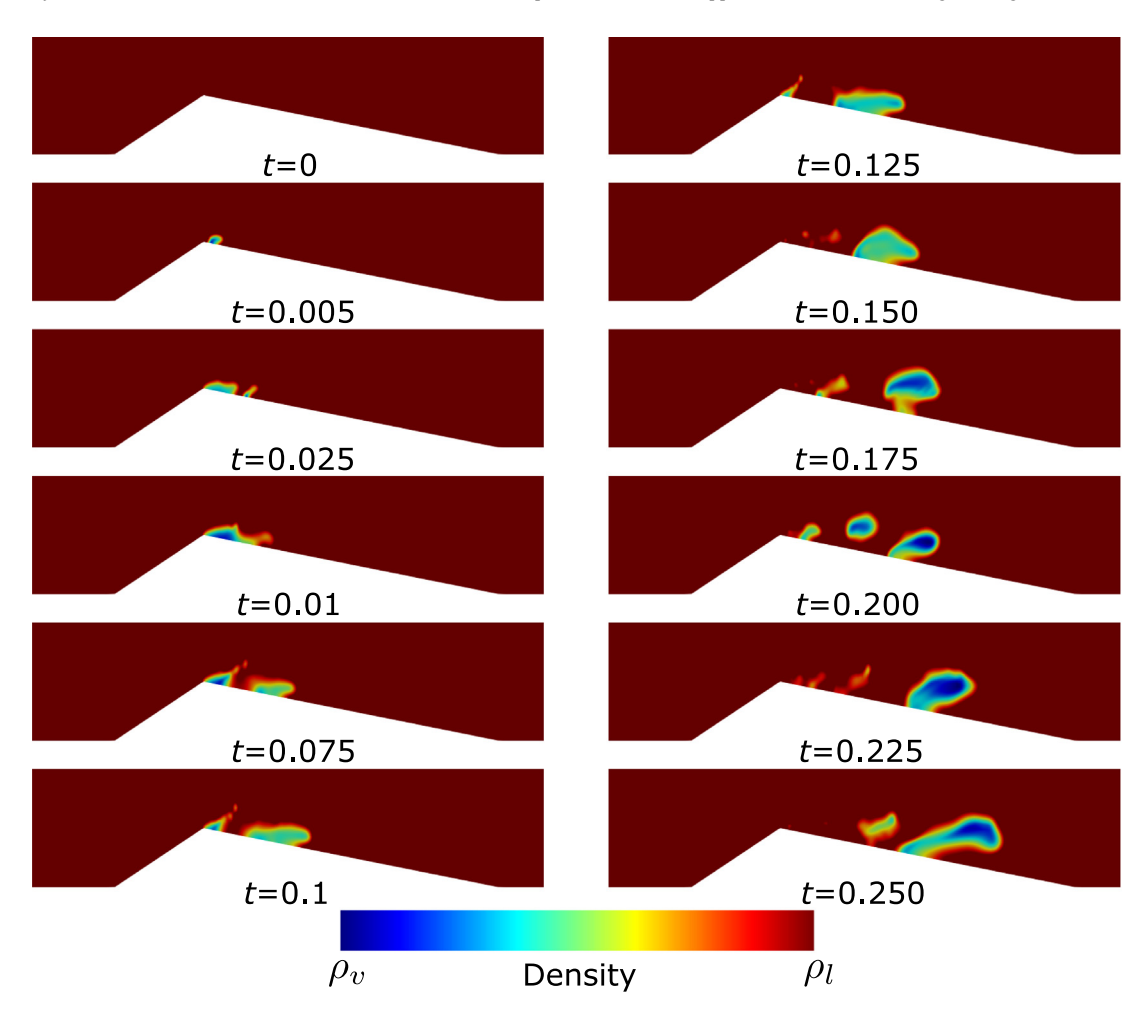


Fig. 10. Density contours for flow past a wedge at t = 0, 0.005, 0.025, 0.05, 0.075, 0.1, 0.125, 0.15, 0.175, 0.2, 0.225 and 0.25 s. (For interpretation of the references to color in this figure legend, the reader is referred to the web version of this article.)

we plot the evolution of the density field in the region of the domain where we do not enforce sponge conditions. The flow accelerates in the region adjacent to the leading edges of the solid square, which causes a decrease in pressure and therefore a reduction in density, as seen at t = 0.05 s in Fig. 12. These regions of low density gradually expand along the direction of the flow over time, as shown at t = 0.25 s. Because of the asymmetry in the location of the solid square, the rate of growth and rate of density reduction for the top and bottom cavities are different. At t = 0.5 s, the vapor cavity below the square is larger than the vaporous cavity above the square. However, this trend reverses at t = 1.0 s. The two cavities formed at t = 0.05 s act as cavitation inception sites, and release vapor bubbles in the region behind the square. At t = 1.5 s, these bubbles detach completely from the square and propagate into the liquid, and move further downstream over time. This cyclic release of new vapor bubbles continues over time.

In Fig. 13, we plot the evolution of the vorticity in the domain. At t = 0.05 s, the flow is clockwise above the square and is counter-clockwise in the region below the square. As the width of the region below the square is slightly smaller than the width of the region above it, the flow is accelerated more leading up to the bottom of the square as compared to the top of the square, thereby implying that the vorticity is higher below the square when compared to the value above it, as seen in Fig. 13. The vortical structures do not interact much till t = 0.5 s, when they deform each other, leading to the pattern observed after t = 1.25 s. This complex interaction of the vortices in addition to phase change causes the cyclic and periodic shedding of vapor cavities shown in Fig. 12.

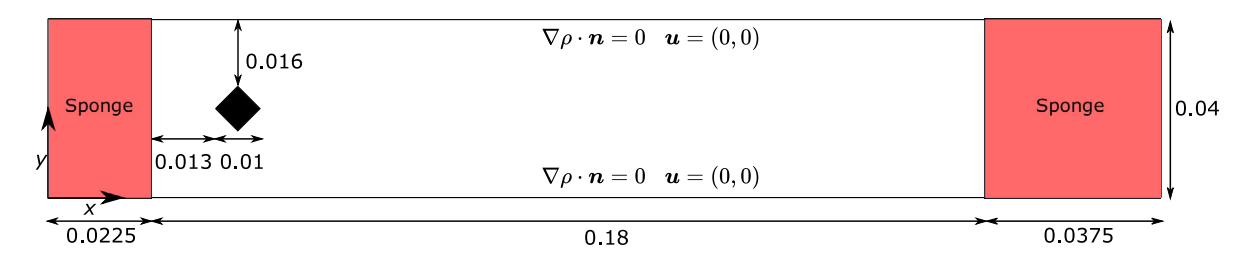


Fig. 11. Computational domain and boundary conditions for flow past a solid square, represented in black. The lengths are in metres.

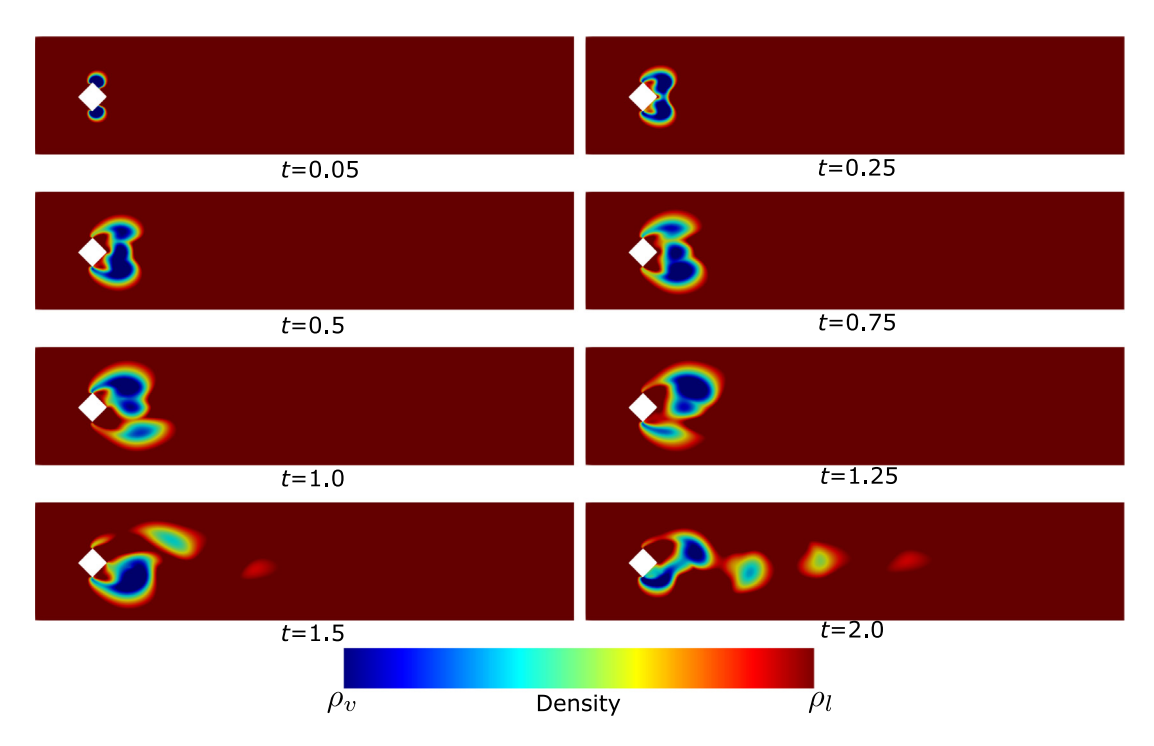


Fig. 12. Density contours for flow past a square obstacle at t = 0.05, 0.25, 0.5, 0.75, 1.0, 1.25, 1.5 and 2.0 s.

6. Conclusions and future work

In this paper, we present a numerical algorithm for the simulation of Navier–Stokes–Korteweg equations, which are phase-field equations that govern the dynamics of liquid–vapor two phase flows. We propose an approach to enlarge the two-phase interface between liquid and vapor by modifying the equation of state in the binodal region using B-spline functions. Using our enlargement strategy, the chemical potential remains differentiable at the binodal boundaries. We argue that this approach improves the stability of the algorithm. Our enlargement strategy can be used to produce up to 10⁸-fold interface enlargements with less than 0.01% error in surface tension. Then, we propose a discretization of the Navier–Stokes–Korteweg equations using the Taylor–Galerkin approach. In the context of this work, this discretization method is advantageous because it does not require knowledge of the eigenvalues of the isentropic form of the NSK equations; a key requirement for most compressible flow solvers. Additionally, it increases the stability and accuracy while solving advection dominated problems, which are frequently encountered when we are dealing with cavitation inception. We also propose a residual-based discontinuity capturing scheme inspired by the Brenner Navier–Stokes equations and an artificial viscosity scheme using spatial filtering to provide additional stability and help in shock capturing. We show the robustness, stability and accuracy of our numerical formulation by solving for manufactured solutions in 1D and 2D, simulating the oscillation of an interface at the two phase junction of an inviscid fluid, studying advection dominated scenarios

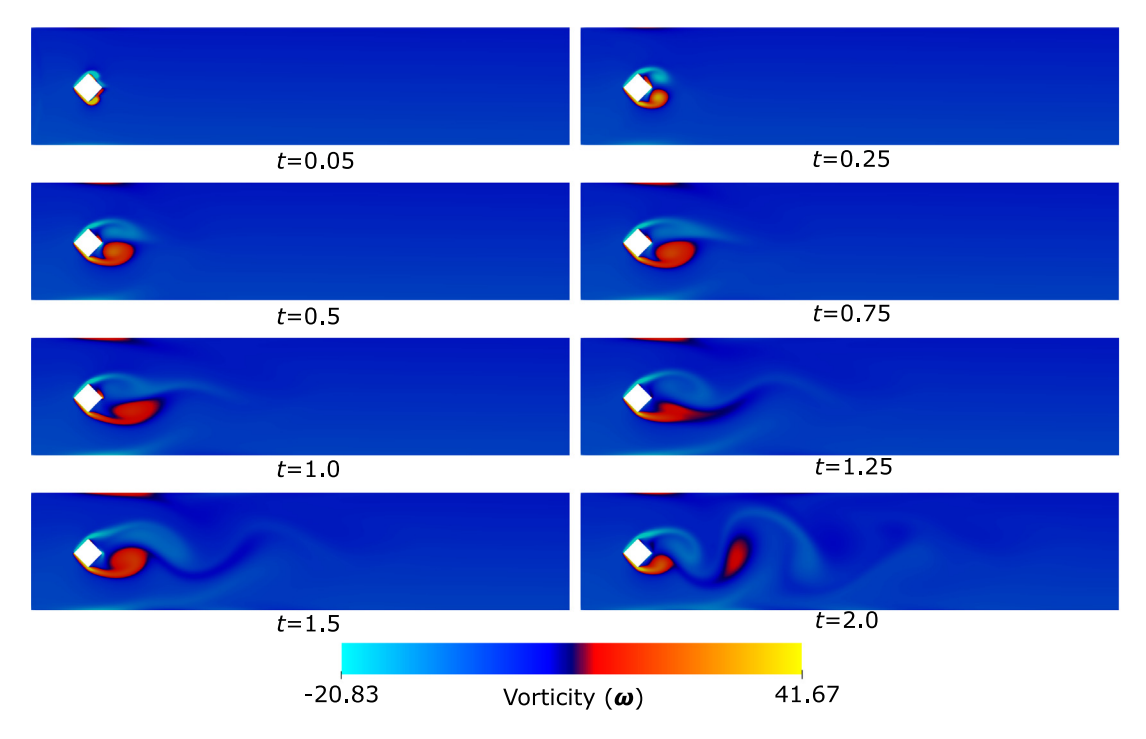


Fig. 13. Vorticity magnitude contours for flow past a square obstacle at t = 0.05, 0.25, 0.5, 0.75, 1.0, 1.25, 1.5 and 2.0 s.

with spatial refinement and then solving benchmark cases such as flow past a wedge and flow past a solid obstacle. We qualitatively capture the flow features observed in experiments of cavitation for both of these cases.

The paper illustrates the potential of the diffuse interface approach while dealing with problems of cavitation inception at large length scales, and presents opportunities to understand cavitation in engineering applications like electronic cooling [72], additive manufacturing [73,74] or thermal management in rechargeable batteries [75]. In the future, we will extend the work to account for the presence of non-condensable gases [76–78] and thermal gradients.

Declaration of competing interest

The authors declare that they have no known competing financial interests or personal relationships that could have appeared to influence the work reported in this paper.

Data availability

Data will be made available on request.

Acknowledgments

We gratefully acknowledge the support from U.S. Department of Defense under the DEPSCoR program (Award No. FA9550-20-1-0165, PO Dr. Yin Lu (Julie) Young) and by the National Science Foundation, United States (Award No. CBET 1805817). This work uses the Bridges-2 system at the Pittsburgh Supercomputing Center (PSC) through allocation #MCH220014 from the Advanced Cyberinfrastructure Coordination Ecosystem: Services & Support (ACCESS) program, which is supported by National Science Foundation, United States grants #2138259, #2138286, #2138307, #2137603, and #2138296. The opinions, findings, and conclusions, or recommendations expressed are those of the authors and do not necessarily reflect the views of the funding agencies.

References

- [1] H. Honda, J. Wei, Enhanced boiling heat transfer from electronic components by use of surface microstructures, Exp. Therm Fluid Sci. 28 (2–3) (2004) 159–169.
- [2] C.E. Brennen, Cavitation in medicine, Interface focus 5 (5) (2015) 20150022.
- [3] P. Horgue, C. Soulaine, J. Franc, R. Guibert, G. Debenest, An open-source toolbox for multiphase flow in porous media, Comput. Phys. Comm. 187 (2015) 217–226.
- [4] A. Asnaghi, A. Feymark, R. Bensow, Improvement of cavitation mass transfer modeling based on local flow properties, Int. J. Multiph. Flow. 93 (2017) 142–157.
- [5] A. Bayram, A. Korobenko, Variational multiscale framework for cavitating flows, Comput. Mech. 66 (2020) 49-67.
- [6] A. Bayram, A. Korobenko, A numerical formulation for cavitating flows around marine propellers based on variational multiscale method, Comput. Mech. 68 (2) (2021) 405–432.
- [7] A. Gnanaskandan, K. Mahesh, A numerical method to simulate turbulent cavitating flows, Int. J. Multiph. Flow. 70 (2015) 22-34.
- [8] Y. Saito, R. Takami, I. Nakamori, T. Ikohagi, Numerical analysis of unsteady behavior of cloud cavitation around a NACA0015 foil, Comput. Mech. 40 (2007) 85–96.
- [9] A.H. Koop, H. Hoeijmakers, Numerical Simulatin of Unsteady Three-Dimensional Sheet Cavitation, University of Twente Enschede, The Netherlands, 2008.
- [10] S.A. Mäkiharju, H. Ganesh, S.L. Ceccio, The dynamics of partial cavity formation, shedding and the influence of dissolved and injected non-condensable gas, J. Fluid Mech. 829 (2017) 420–458.
- [11] S. Frikha, O. Coutier-Delgosha, J.A. Astolfi, Influence of the cavitation model on the simulation of cloud cavitation on 2D foil section, Int. J. Rotating Mach. 2008 (2008).
- [12] J.D. Van der Waals, The thermodynamic theory of capillarity under the hypothesis of a continuous variation of density, J. Stat. Phys. 20 (2) (1979) 200–244.
- [13] B.D. Coleman, W. Noll, The thermodynamics of elastic materials with heat conduction and viscosity, Arch. Ration. Mech. Anal. 13 (1) (1963) 167–178.
- [14] D. Diehl, J. Kremser, D. Kröner, C. Rohde, Numerical solution of Navier-Stokes-Korteweg systems by local discontinuous Galerkin methods in multiple space dimensions, Appl. Math. Comput. 272 (2016) 309-335.
- [15] J. Neusser, C. Rohde, V. Schleper, Relaxation of the Navier–Stokes–Korteweg equations for compressible two-phase flow with phase transition, Internat. J. Numer. Methods Fluids 79 (12) (2015) 615–639.
- [16] L. Tian, Y. Xu, J. Kuerten, J.J. van der Vegt, A local discontinuous Galerkin method for the (non)-isothermal Navier–Stokes–Korteweg equations, J. Comput. Phys. 295 (2015) 685–714.
- [17] P. Germain, P. LeFloch, Finite energy method for compressible fluids: The Navier-Stokes-Korteweg model, Comm. Pure Appl. Math. 69 (1) (2016) 3-61.
- [18] H. Gomez, T.J. Hughes, X. Nogueira, V.M. Calo, Isogeometric analysis of the isothermal Navier–Stokes–Korteweg equations, Comput. Methods Appl. Mech. Engrg. 199 (25–28) (2010) 1828–1840.
- [19] J. Liu, H. Gomez, J.A. Evans, T.J. Hughes, C.M. Landis, Functional entropy variables: a new methodology for deriving thermodynamically consistent algorithms for complex fluids, with particular reference to the isothermal Navier–Stokes–Korteweg equations, J. Comput. Phys. 248 (2013) 47–86.
- [20] L. Tian, Y. Xu, J.G. Kuerten, J.J. van der Vegt, An h-adaptive local discontinuous Galerkin method for the Navier-Stokes-Korteweg equations, J. Comput. Phys. 319 (2016) 242–265.
- [21] T. Hitz, J. Keim, C.-D. Munz, C. Rohde, A parabolic relaxation model for the Navier-Stokes-Korteweg equations, J. Comput. Phys. 421 (2020) 109714.
- [22] V.I. Levitas, M. Javanbakht, Surface tension and energy in multivariant martensitic transformations: phase-field theory, simulations, and model of coherent interface, Phys. Rev. Lett. 105 (16) (2010) 165701.
- [23] J. Kim, Phase-field models for multi-component fluid flows, Commun. Comput. Phys. 12 (3) (2012) 613-661.
- [24] X. Mao, V. Joshi, R. Jaiman, A variational interface-preserving and conservative phase-field method for the surface tension effect in two-phase flows, J. Comput. Phys. 433 (2021) 110166.
- [25] D. Jamet, O. Lebaigue, N. Coutris, J. Delhaye, The second gradient method for the direct numerical simulation of liquid-vapor flows with phase change, J. Comput. Phys. 169 (2) (2001) 624-651.
- [26] D. Nayigizente, S. Ducruix, T. Schmitt, Development of an interface thickening method for the direct numerical simulation of compressible liquid-vapor flows in the framework of the second gradient theory, Phys. Fluids 33 (5) (2021) 052119.
- [27] T. Hu, H. Wang, H. Gomez, Direct van der waals simulation (DVS) of phase-transforming fluids, Sci. Adv. 9 (11) (2023) eadg3007.
- [28] J. Donea, A taylor-Galerkin method for convective transport problems, Internat. J. Numer. Methods Engrg. 20 (1) (1984) 101-119.
- [29] P. Amestoy, R. Tilch, Solving the compressible Navier-Stokes equations with finite elements using a multifrontal method, IMPACT Comput. Sci. Eng. 1 (1) (1989) 93–107.
- [30] D. Ambrosi, L. Quartapelle, A Taylor-Galerkin method for simulating nonlinear dispersive water waves, J. Comput. Phys. 146 (2) (1998) 546-569.
- [31] H. Brenner, Navier-Stokes revisited, Physica A Stat. Mech. Appl. 349 (1-2) (2005) 60-132.
- [32] J. Upperman, N.K. Yamaleev, Entropy stable artificial dissipation based on Brenner regularization of the Navier-Stokes equations, J. Comput. Phys. 393 (2019) 74–91.
- [33] T. Schmitt, Large-eddy simulations of the Mascotte test cases operating at supercritical pressure, Flow Turbul. Combust. 105 (1) (2020) 159–189.
- [34] E. Rood, Mechanisms of cavitation inception, 1991.

- [35] H. Gomez, K.G. van der Zee, Computational phase-field modeling, in: Encyclopedia of Computational Mechanics, 2017.
- [36] D.-Y. Peng, D.B. Robinson, A new two-constant equation of state, Ind. Eng. Chem. Fundam. 15 (1) (1976) 59-64.
- [37] G.M. Kontogeorgis, E.C. Voutsas, I.V. Yakoumis, D.P. Tassios, An equation of state for associating fluids, Ind. Eng. Chem. Res. 35 (11) (1996) 4310–4318.
- [38] G. Soave, Improvement of the van der Waals equation of state, Chem. Eng. Sci. 39 (2) (1984) 357-369.
- [39] M. Plapp, Unified derivation of phase-field models for alloy solidification from a grand-potential functional, Phys. Rev. E 84 (3) (2011) 031601
- [40] F. Magaletti, L. Marino, C.M. Casciola, Shock wave formation in the collapse of a vapor nanobubble, Phys. Rev. Lett. 114 (6) (2015) 064501.
- [41] A. Martínez, L. Ramírez, X. Nogueira, S. Khelladi, F. Navarrina, A high-order finite volume method with improved isotherms reconstruction for the computation of multiphase flows using the Navier–Stokes–Korteweg equations, Comput. Math. Appl. 79 (3) (2020) 673–696.
- [42] C. De Boor, C. De Boor, A Practical Guide to Splines, vol. 27, springer-verlag New York, 1978.
- [43] A. Chertock, P. Degond, J. Neusser, An asymptotic-preserving method for a relaxation of the Navier-Stokes-Korteweg equations, J. Comput. Phys. 335 (2017) 387-403.
- [44] C.M. Elliott, S. Larsson, Error estimates with smooth and nonsmooth data for a finite element method for the Cahn-Hilliard equation, Math. Comp. 58 (198) (1992) 603–630.
- [45] K. Ammar, B. Appolaire, G. Cailletaud, F. Feyel, S. Forest, Finite element formulation of a phase field model based on the concept of generalized stresses, Comput. Mater. Sci. 45 (3) (2009) 800–805.
- [46] P. Nadukandi, E. Oñate, J. Garcia, A high-resolution Petrov–Galerkin method for the 1D convection–diffusion–reaction problem, Comput. Methods Appl. Mech. Engrg. 199 (9–12) (2010) 525–546.
- [47] T.J. Hughes, Recent progress in the development and understanding of SUPG methods with special reference to the compressible Euler and Navier-Stokes equations, Internat. J. Numer. Methods Fluids 7 (11) (1987) 1261–1275.
- [48] A.A. Oberai, J. Liu, D. Sondak, T. Hughes, A residual based eddy viscosity model for the large eddy simulation of turbulent flows, Comput. Methods Appl. Mech. Engrg. 282 (2014) 54–70.
- [49] T.J. Hughes, L.P. Franca, G.M. Hulbert, A new finite element formulation for computational fluid dynamics: VIII. The Galerkin/least-squares method for advective-diffusive equations, Comput. Methods Appl. Mech. Engrg. 73 (2) (1989) 173–189.
- [50] O. Colin, M. Rudgyard, Development of high-order Taylor-Galerkin schemes for LES, J. Comput. Phys. 162 (2) (2000) 338-371.
- [51] M. Philip, M. Boileau, R. Vicquelin, T. Schmitt, D. Durox, J.-F. Bourgouin, S. Candel, Ignition sequence of an annular multi-injector combustor, Phys. Fluids 26 (9) (2014) 091106.
- [52] M. Pelletier, T. Schmitt, S. Ducruix, A multifluid Taylor-Galerkin methodology for the simulation of compressible multicomponent separate two-phase flows from subcritical to supercritical states, Comput. & Fluids 206 (2020) 104588.
- [53] M.K. Kadalbajoo, P. Arora, Taylor-Galerkin B-spline finite element method for the one-dimensional advection-diffusion equation, Numer. Methods Partial Differential Equations 26 (5) (2010) 1206–1223.
- [54] T. Colonius, Modeling artificial boundary conditions for compressible flow, Annu. Rev. Fluid Mech. 36 (2004) 315-345.
- [55] J. Mathew, R. Lechner, H. Foysi, J. Sesterhenn, R. Friedrich, An explicit filtering method for large eddy simulation of compressible flows, Phys. Fluids 15 (8) (2003) 2279–2289.
- [56] S. Stolz, N.A. Adams, An approximate deconvolution procedure for large-eddy simulation, Phys. Fluids 11 (7) (1999) 1699-1701.
- [57] D.E. Fyfe, E.S. Oran, M. Fritts, Surface tension and viscosity with Lagrangian hydrodynamics on a triangular mesh, J. Comput. Phys. 76 (2) (1988) 349–384.
- [58] G. Soave, Equilibrium constants from a modified Redlich-Kwong equation of state, Chem. Eng. Sci. 27 (6) (1972) 1197-1203.
- [59] A. Gnanaskandan, K. Mahesh, Large eddy simulation of the transition from sheet to cloud cavitation over a wedge, Int. J. Multiph. Flow. 83 (2016) 86–102.
- [60] J.H. Seo, S. Lele, Numerical investigation of cloud cavitation and cavitation noise on a hydrofoil section, 2009, CAV2009-62.
- [61] H. Ganesh, Bubbly Shock Propagation as a Cause of Sheet to Cloud Transition of Partial Cavitation and Stationary Cavitation Bubbles Forming on a Delta Wing Vortex. (Ph.D. thesis), The University of Michigan, 2015.
- [62] T. Pham, F. Larrarte, D.H. Fruman, Investigation of unsteady sheet cavitation and cloud cavitation mechanisms, J. Fluids Eng. 121 (2) (1999) 289–296.
- [63] V.I. Vlasov, S.L. Skorokhodov, Analytical solution for the cavitating flow over a wedge. I, Comput. Math. Math. Phys. 60 (2020) 2032–2055.
- [64] V.I. Vlasov, S.L. Skorokhodov, Analytical solution for the cavitating flow over a wedge. II, Comput. Math. Math. Phys. 61 (11) (2021) 1834–1854.
- [65] M. Morgut, E. Nobile, I. Biluš, Comparison of mass transfer models for the numerical prediction of sheet cavitation around a hydrofoil, Int. J. Multiph. Flow. 37 (6) (2011) 620–626.
- [66] A. Niedźwiedzka, G.H. Schnerr, W. Sobieski, Review of numerical models of cavitating flows with the use of the homogeneous approach, Arch. Thermodyn. 37 (2) (2016).
- [67] T. Leighton, M. Farhat, J. Field, F. Avellan, Cavitation luminescence from flow over a hydrofoil in a cavitation tunnel, J. Fluid Mech. 480 (2003) 43–60.
- [68] S. Mittal, Control of flow past bluff bodies using rotating control cylinders, J. Fluids Struct. 15 (2) (2001) 291–326.
- [69] W. Rodi, On the simulation of turbulent flow past bluff bodies, J. Wind Eng. Ind. Aerodyn. 46 (1993) 3-19.
- [70] D.J. Tritton, Experiments on the flow past a circular cylinder at low Reynolds numbers, J. Fluid Mech. 6 (4) (1959) 547-567.
- [71] J. Katz, T. O'hern, Cavitation in large scale shear flows, J. Fluids Eng. 108 (3) (1986) 373-376.

- [72] M. Bongarala, H. Hu, J.A. Weibel, S.V. Garimella, Microlayer evaporation governs heat transfer enhancement during pool boiling from microstructured surfaces, Appl. Phys. Lett. 120 (22) (2022) 221602.
- [73] Q. Zhu, J. Yan, A mixed interface-capturing/interface-tracking formulation for thermal multi-phase flows with emphasis on metal additive manufacturing processes, Comput. Methods Appl. Mech. Engrg. 383 (2021) 113910.
- [74] S. Lin, Z. Gan, J. Yan, G.J. Wagner, A conservative level set method on unstructured meshes for modeling multiphase thermo-fluid flow in additive manufacturing processes, Comput. Methods Appl. Mech. Engrg. 372 (2020) 113348.
- [75] J. Luo, D. Zou, Y. Wang, S. Wang, L. Huang, Battery thermal management systems (BTMs) based on phase change material (PCM): A comprehensive review, Chem. Eng. J. 430 (2022) 132741.
- [76] S. Mukherjee, H. Gomez, Flow and mixing dynamics of phase-transforming multicomponent fluids, Appl. Phys. Lett. 115 (10) (2019) 104101.
- [77] S. Mukherjee, H. Gomez, Understanding how non-condensable gases modify cavitation mass transfer through the van der Waals theory of capillarity, Appl. Phys. Lett. 117 (20) (2020) 204102.
- [78] S. Mukherjee, H. Gomez, Effect of dissolved gas on the tensile strength of water, Phys. Fluids 34 (12) (2022) 126112.